



LIBRARY Michigan State University

This is to certify that the

thesis entitled

Examination of Dislocation Structures in B2 Stiochiometric NiAl Alloys using TEM and SEM Techniques

presented by

Boon-Chai Ng

has been accepted towards fulfillment of the requirements for

Master's degree in Materials Science

Major professor

Date May 6, 1997

O-7639

MSU is an Affirmative Action/Equal Opportunity Institution

PLACE IN RETURN BOX to remove this checkout from your record. TO AVOID FINES return on or before date due.

DATE DUE	DATE DUE	DATE DUE

MSU is An Affirmative Action/Equal Opportunity Institution ctoirclaisedus.pm3-p.1

EXAMINATION OF DISLOCATION STRUCTURES IN B2 STOICHIOMETRIC NIAI ALLOYS USING TEM AND SEM TECHNIQUES

By

Boon-Chai Ng

A THESIS

Submitted to
Michigan State University
in partial fulfillment of the requirements
for the degree of

MASTERS OF SCIENCE

Department of Materials Science and Mechanics

1997

ABSTRACT

EXAMINATION OF DISLOCATION STRUCTURES IN B2 STOICHIOMETRIC NIAI ALLOYS USING TEM AND SEM TECHNIQUES

By

Boon-Chai Ng

Toughened and embrittled single crystals of stoichiometric NiAl alloys were examined using TEM and SEM. It is observed that air cooling has a profound impact on the yield strength and the mobility of the dislocations whereas furnace cooling results in severe embrittlement. Furnace cooled specimens exhibit dislocations that are heavily tangled whereas air cooled specimens exhibit much fewer dislocation tangles. The electron channeling contrast imaging (ECCI), a scanning electron microscopy technique, is used to examine the dislocation behavior near crack tips of 4-point bend specimens. ECCI imaging of the dislocations ahead of the crack tips show that the number of dislocations and their distribution ahead of the crack tips for air cooled specimens are much more than that of the furnace cooled specimens. This is because there are more mobile dislocations and fewer pinned dislocations in the air cooled specimens, hence pre-existing and newly generated dislocations will be able to move farther away from the crack tip than when they are pinned due to furnace cooling.

ACKNOWLEDGEMENTS

This thesis would never have been made possible if not for the many individuals who were there to help and guide me in one way or another. Among the many individuals, I would like to single out a few to express my sincere thanks.

I would like to thank my advisor, Dr. Martin A. Crimp for his guidance and for his many helpful suggestions and painstaking reviews during the preparation of this thesis. His dedication, easy going and ever believing that I "will always do a good job" have been an inspiration to me. A fine mentor!

I would like to thank the Office of Naval Research and Dr. George Yoder (Scientific Officer) for their funding and support (Grant No. N00014-94-1-0204), the National Science Foundation (Grant No. DMR#9302040) and Michigan State University for providing the funds for the purchase of the CamScan 44 FE FEG-SEM used in this study.

Thanks to Dr. Ram Darolia at General Electric Aircraft Engine Division for the supply of NiAl single crystals.

Special mention goes to Benjamin Andrews Simkin, who was instrumental in my acquiring the ECCI technique, and Biman Ghosh, for his assistance in analyzing the

dislocation structures. Special thanks to Alan Gibson for proof reading the first draft of this paper.

Last but not least, thanks to members of my thesis committee, Dr. D.S. Grummon and Dr. T.R. Bieler for their time and helpful suggestions.

TABLE OF CONTENT

LIST OF TABLES	v i
LIST OF FIGURES	vii
CHAPTER 1: INTRODUCTION	1
1.1 Introduction	1
1.2 RECENT STUDIES	
1.3 SLIP SYSTEMS IN NIAL	16
1.4 OBSERVATION OF DISLOCATIONS IN ENHANCED PLASTICITY IN NIAL	17
1.5 OBJECTIVE	18
CHAPTER 2: TEM EXAMINATION	19
2.1 Experimental Procedure	19
2.2 SLIP TRACE ANALYSIS	22
2.3 DISLOCATION ANALYSIS	25
2.4 Results	25
2.4.1 Undeformed Specimens	
2.4.2 DEFORMED SPECIMENS	32
2.5 COMPUTER SIMULATION	45
2.6 Summary	51
CHAPTER 3: SEM EXAMINATION	53
3.1 Introduction to electron channeling contrast imaging (ECCI)	53
3.2 Experimental Procedure	
3.3 Results	60
3.4 SUMMARY	75
CHAPTER 4: DISCUSSION	76
CHAPTER 5: GENERAL CONCLUSION	80
REFERENCES	82

LIST OF TABLES

Table 1: Properties of test specimens	27
Table 2: Burgers vector analyzed for each of the tested specimens in	
correlation to their heat treatment histories and yield strength	38
Table 3: Parameters used in simulating dislocation "A"	50

LIST OF FIGURES

Figure 1: B2 structure is the ordered bcc lattice. Two kinds of atoms (A and B) occupy corner positions or body center position respectively	
Figure 2: Phase diagram illustrating the atomic structure as a function of temperature for the Ni-Al alloy system	4
Figure 3: Plot of thermal conductivity for Ni-50Al in comparison to a typical Ni-based superalloy as a function of temperature. Adapted from [2]	5
Figure 4: Cracks propagate by a combination of plastic and elastic process. Plastic portion of the crack is created by the dislocations. Elastic portion of the crack is a result of brittle fracture of the dfz.	12
Figure 5: The emitted dislocations exert a back stress to the crack tip thus reducing the local stress intensity factor k. Stress relaxation is viewed as a result of an increase of the total number of dislocations within the plastic zone	14
Figure 6: Crack, the dislocation free zone and plastic zone in an infinite elastic medium. f(x) is the distribution function of the dislocations. Adapted from [22]	18
Figure 7: Orientation of specimen within the sterographic triangle.	20
Figure 8: Flow chart of the heat treatment procedure	21
Figure 9: Two faces of a deformed specimen showing the slip planes with measured angles α and β	23
Figure 10: Schematic representation of a compression sample displaying the measurement of α and β used in determining the slip plane.	24
Figure 11: Sterographic projection of the specimen displaying the angles α and β used to determine the slip plane	26
Figure 12: Burgers vector analysis for undeformed 673FC specimen. The same area is shown with different operative reflections[011], [200] and [110]	29

Figure 13: Microsgraphs of a) 473FC specimen and b) 673AC specimens displaying both <001> and <011> dislocations	30
Figure 14: Single dislocations that are widely spaced with few dislocation loops and tangles were observed in a) undeformed specimen, b) undeformed 673FC specimen and c) undeformed 673AC specimen	31
Figure 15: Burgers vector analysis for deformed 673AC specimen shows both "a" dislocations with $\mathbf{b} = [\ 1\ 0\ 0\]$ and "b" dislocations with $\mathbf{b} = [\ 0\ 1\ \overline{1}]$ present. The same region with different operative refelctions area shown: a) $[\ 1\ \overline{1}\ 0\]$, b) $[\ 2\ 0\ 0\]$, c) $[\ 2\ \overline{1}\ \overline{1}\]$	33
Figure 16: Burgers vector analysis revealed both $\mathbf{b} = [\ \overline{1} \ 0 \ 0 \]$ and $\mathbf{b} = [\ 0 \ 1 \ \overline{1} \]$ dislocations present in deformed 673FC specimen. The same area is shown with different operative reflections a) $[\ \overline{1} \ 1 \ 0 \]$, b) $[\ 0 \ 1 \ \overline{1} \]$, c) $[\ 0 \ 2 \ 0 \]$	34
Figure 17: Micrographs of deformed 473FC specimen displaying both <001> and <011) dislocations. 'a' denotes <001> and 'b' denotes <011>	35
Figure 18: <001> and <011> dislocations were observed in deformed 1590FC specimen. 'a' denotes <011> and 'b' denoted <011>	36
Figure 19: Burgers vector analysis reveals both <001> and <011> dislocations present in deformed 1590AC specimens. 'a' denotes <001> and 'b' denotes <011>	37
Figure 20: Dislocations were observed to be heavily tangled in deformed 473FC specimen. a) brightfield image and b) weak beam image	40
Figure 21: Dislocations were observed to be heavily in deformed 1590FC specimen. a) brightfield image and b) weak beam image	41
Figure 22: Dislocations were observed to have less tangles in deformed 673FC specimen. a) brightfield image and b) weak beam image	42
Figure 23: Very few dislocation tangles were observed in deformed 1590AC specimens. a) brightfield image and b) weak beam image	43
Figure 24: Very few dislocation tangles were obsreved in dformed 1590AC specimens. a) brightfield image and b) weak beam image	44
Figure 25: Dislocation mark "A" in an undeformed 673AC specimen which will be used to illustrate the technique of defect identification by image matching	48
Figure 26: A set of experimental images (a) - (g) of dislocation "a" of 673AC speciemen take with the diffraction conditions given in Table 3 and four sets	

of computed images for the same diffraction conditions corresponding to the burgers ½ [101] and ½ [110]	49
Figure 27: Near surface defects will cause a change in the bse yield due to variation from the bragg condition	55
Figure 28: Selected area channeling pattern (SACP)	57
Figure 29: Ray diagrams illustrating schematically the scanning action in the selected area channeling pattern (SACP)	58
Figure 30: Schematic diagram of a 4-point bend sample showing the notch plane and the notch direction	59
Figure 31: Schematic diagram showing the notched sample in the 4-point bend fixture attached to the E. Fullan deformation stage.	61
Figure 32: SACP showing a) a zone axis, b) tilting to one of the channeling band c) final adjustment of aligning the edge of the band (Bragg condition) to the microscope axis	62
Figure 33 Crack tip in deformed specimen 673AC under different imaging conditions. a) high magnification SE image of the crack tip region. inserted image shows a low magnification SE image of the secondary crack and highlighting the area analyze. b) ECCI image of the crack tip region showing dislocaitons lying end-on.	64
Figure 34 Examples of dislocation distribution left in the wake of the cracks for 1590FC specimen. a) SE image of the crack edge, b) ECCI image of the same crack edge region.	65
Figure 35: A higher bse yield resulted when the rastering beam is near to a edge of a specimen.	67
Figure 36: Schematic diagram showing how the combination of mode I and II tear results in a change in the BSE yield for both sides of the crack edge	68
Figure 37: Images of a crack edge of a 673AC specimen illustrating a) SE image and b) ECCI image with dislocations in dark/bright contrast lying end-on	69
Figure 38: Images of an area 80 µm from the edge of the crack for specimen 673AC before (a) and after (b) 4 point bend test. no significant change in the dislocation density was observed.	71
Figure 39: Comparsion of dislocation densities for a) 673AC specimens, b) 673FC specimen and c) 1590FC specimen	72

Figure 40: Changes in contrast of dislocation images when the channeling	
band is changed from a) +g to b) - g	73
6	
Figure 41: Cracks do no show any change in contrast as the channeling	
condition changes from + g to - g	74

CHAPTER 1

INTRODUCTION

1.1 Introduction

One of the greatest challenges currently facing the materials community is the need to develop a new generation of materials to replace Ni-based superalloys in the hot section of gas-turbine engines for aircraft-propulsion systems. The present alloys, which have a Ni-based solid solution matrix surrounding Ni₃Al-based precipitates, are currently used at temperatures exceeding 1373 K. Since Ni₃Al melts at 1669 K and Ni at 1726 K, it is clear that significantly higher operating temperatures with improvement in efficiency and thrust-to-weight ratio can only be attained by the development of an entirely new material system [1]. This problem is a primary reason for the current high level of interest in high temperature intermetallic compounds.

A high melting temperature is the first and most obvious requirement for the new generation of materials since the melting temperature must exceed the operating temperature. Low density is very important since the weight of the propulsion system as a whole decreases rapidly with decreasing weight of the rotating components [2]. Oxidation resistance at high temperature is also critical as are cost considerations. In addition, the material must possess some intrinsic plasticity and toughness (the required

levels of which are not yet totally clear [1]). However, some plasticity at room temperature is required for fit-up of the components during assembly.

Intermetallic compounds have the requisite combination of properties to satisfy some of the list of requirements just described. An intermetallic compound is a true compound of two or more metals that has a distinctive structure in which the metallic constituents are in relatively fixed stoichiometic ratios and are usually ordered on two or more sublattices, each with its own distinct population of atoms [3]. Among the intermetallic compounds currently being studied, NiAl has been the subject of the most study and development.

NiAl possesses the ordered cubic B2 (space group Pm $\overline{3}$ m, CsCl prototype) crystal structure. This structure consists of two interpenetrating primitive cubic cells (Figure 1), where Al atoms occupy the cube corners of one sublattice and Ni atoms occupy the cube corners of the second sublattice. The Ni-Al binary equilibrium phase diagram [4] is shown in Figure 2. NiAl exhibits a wide single phase field, and the stoichiometric composition melts congruently at 1911 K.

NiAl offers many advantages: (1) density of 5.95 g/cm³, approximately 2/3 that of Ni-based superalloys, (2) thermal conductivity that is four to eight times that of Ni-based superalloys (Figure 3), (3) excellent oxidation resistance, (4) simple, ordered body-centered-cubic derivative B2, (CsCl) crystal structure, (5) lower ductile to brittle transition temperature (DBTT) relative to other intermetallic alloys, (6) high melting temperature that is approximately 573 K higher that Ni-based superalloys, (7) relatively easy process-ability by conventional melting, and powder-and metal forming techniques,

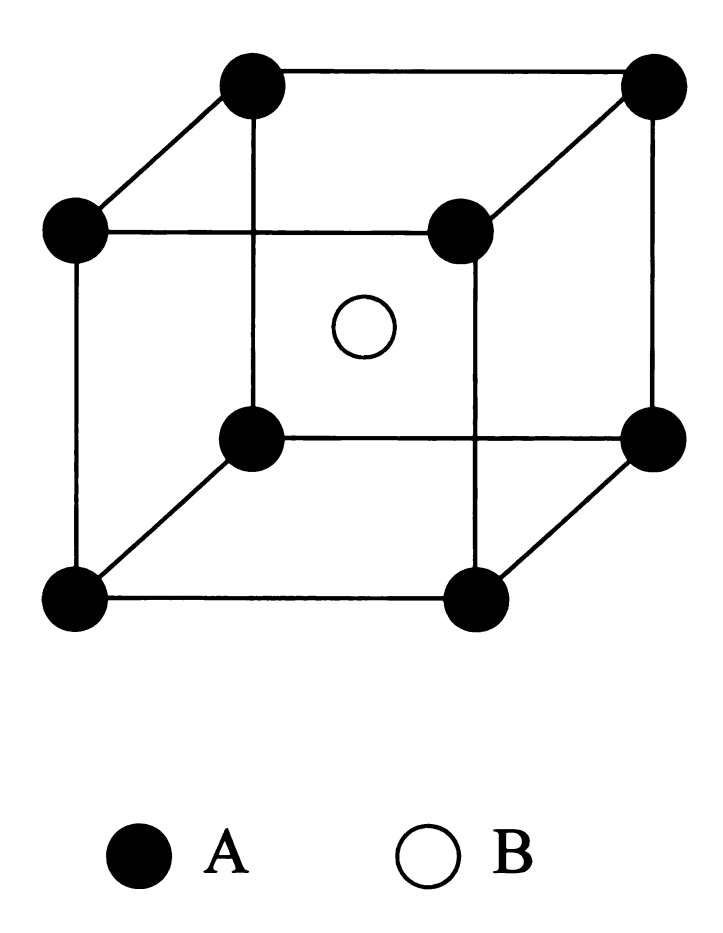


Figure 1. B2 structure is the ordered bcc lattice. Two kinds of atoms (A and B) occupy corner positions or body center position respectively.

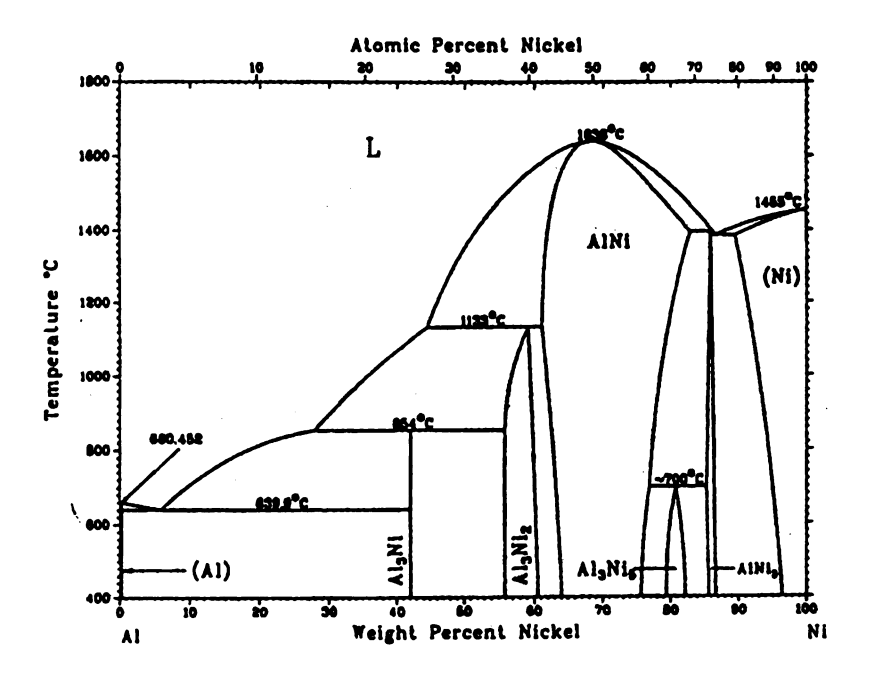


Figure 2. Phase diagram illustrating the atomic structure as a function of temperature for the Ni-Al alloy system. Adapted from [4].

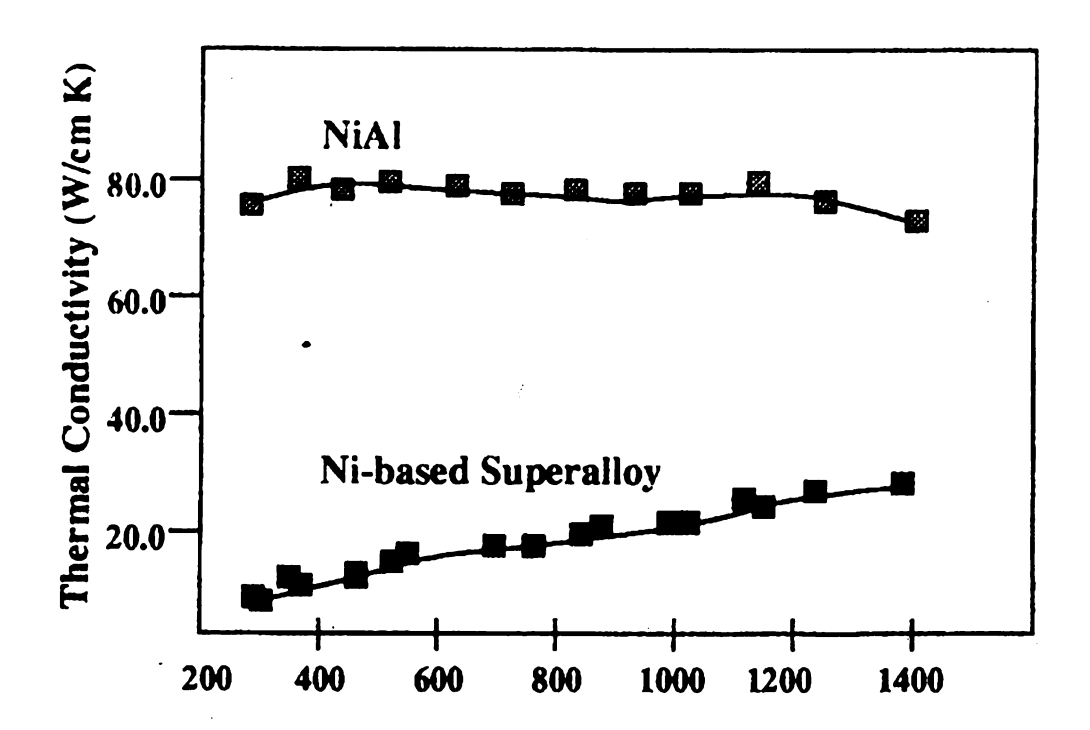


Figure 3. Plot of thermal conductivity for Ni-50Al in comparison to a typical Ni-based superalloy as a function of temperature. Adapted from [2].

and (8) high Young's modulus relative to Ni-based superalloys. For a review of the properties of NiAl, see ref. [5].

The use of NiAl as structural members, however, suffers from two major drawbacks: (1) poor ductility and toughness at ambient temperatures and (2) low strength and creep at elevated temperatures [6,7]. Because of the excellent high-temperature capability of NiAl, considerable effort has been devoted to understanding brittle fracture and improving mechanical properties of NiAl during the past years. These will be covered in the following pages.

1.2 Recent Studies of NiAl

Several recent studies have shown that it is possible to improve the room temperature properties of near-stoichiometric NiAl single crystals.

Hack et al. [8,9] have recently reported some interesting results that contribute to our understanding of deformation and fracture in single crystal NiAl. Their studies indicate that the fracture resistance of single crystal NiAl can be dramatically improved by controlled heat treatments. NiAl single crystals that were furnace-cooled from a homogenization treatment at 1590 K exhibited a tensile elongation of 1.0% and a fracture toughness of 2.4 MPa.m^{1/2} at room temperature. The room temperature ductility increased to 7.0% and the toughness increased to 16.7 MPa.m^{1/2} when these crystals were reheated to 673 K followed by air cooling. The beneficial effect of the 673 K heat treatment disappeared as the specimens were cooled slowly inside a furnace. The authors attribute the low ductility and poor toughness of single crystal NiAl to strain-aging embrittlement

involving the pinning of mobile dislocations by interstitials such as carbon and oxygen,

similar to the strain-aging embrittlement in mild steels [10]. The strong interaction between the interstitial C atoms and the cores of dislocations results in a potent strengthening effect for C. At elevated temperatures, the free energy of the solution of C in Fe is lowered by the random distribution of C in solution. As the temperature is lowered, the driving force for the C atoms to diffuse to dislocation cores increases so as to lower the internal energy. If the temperature is lowered rapidly enough to limit redistribution of the C atoms by diffusion, the C remains randomly distributed at low temperatures. However, if the cooling rate allows for ample interstitial diffusion of the C, or the temperature is maintained at a level where the driving force for redistribution is high and diffusion is sufficiently rapid, the bulk of the C atoms can assume positions at or near the cores of dislocations, forming so-called Cottrell atmospheres [11]. The interstitial content in these NiAl crystals is reported to be only about 100 wt. ppm carbon and 50 wt. ppm oxygen. The data [8,9] further suggests that ductility and toughness of NiAl are more strongly dependent upon mobile dislocation density rather than on the inherent mobility of dislocations in the ordered lattice.

The population of mobile dislocations can be affect by the strong interaction between the interstitial solute atoms and the highly strained region at the core of a dislocation [12]. Decoration of the core region with interstitial solutes renders the dislocations immobile, thus reducing the mobile dislocation density. This phenomena is known as strain aging. The strain aging embrittlement in NiAl has been studied by Brzeski et al. [13]. In their studies, compressive load-strain curves for test specimens showed smooth yielding at room temperature and serrated yielding at temperatures between 100 and 200°C during compression testing with the serrations beginning with the onset of the plastic deformation. This is typical of solute drag interactions between the dislocations and interstitial solutes [12]

and is known as dynamic strain aging. It is characterized by the repetitive breaking away from the atmosphere by a dislocation followed by diffusion of the atmosphere to the dislocation where it pins the dislocations again. This leads to the observed serrated yielding in load-strain curves [13].

Strain aging embrittlement is also consistent with observations of recovery of the flow stress and a sharp yield drop in polycrystal NiAl which has been pre-deformed by hydrostatic pressure. Margevicius and Lewandowski [14,15] suppressed premature fracture in tension and compression tests of NiAl alloys by the use of superimposed hydrostatic Both the tension and compression tests, conducted at 0.1 MPa following pressure. pressurization at 500 MPa., reveal a significant effect of pressurization on the subsequent flow stress at 0.1 MPa. The tests showed that flow stresses obtained following pressurization are significantly lower than those obtained on specimens simply tested at 0.1MPa. Such a decrease in flow stress is consistent with the pressure-induced generation of mobile dislocations, either at second phase particles or grain boundaries. Margevicius and Lewandowski [14,15] concluded that dislocations were generated at second phase particles (e.g. impurities or inclusions) in the NiAl or alternatively, at grain boundaries due to the elastic anisotropy of NiAl. In addition to pressure lowering the initial flow stress, specimens tested in tension with 500 MPa pressure exhibited fracture strains in excess of 10% compared to the usual 1-2% [8]. While the pressure-induced generation of mobile dislocations probably explains the former, superimposed pressure greatly reduces the rate of damage accumulation [16], thereby increasing the ductility.

Based on the embrittling mechanism proposed by Hack et al. [8,9], Liu [17], reported that the fracture resistance of NiAl crystals is expected to be effectively improved by either reducing the interstitial content or scavenging interstitial by certain alloying additions.

Microalloying with Fe, Ga, or Mo at levels less than 0.5 atomic % has been reported to increase the room temperature ductility of <110> crystals by as much as 6% [18]. Microalloying with Fe also improves the ductility of <111> crystals and lowers the ductility to brittle transition temperature (DBTT) for <001> crystals. The mechanism by which Fe, Mo and Ga additions enhance the room temperature ductility is not known, although it may be an indirect effect of point defects or impurity gettering by the small additions differences.

While microalloying, pre-straining and alternative heat treatments clearly cause alterations in the initial state of NiAl crystals, there are no changes in operative slip systems and/or significant changes in dislocation substructure following deformation. So it is unclear whether the improvements in ductility and toughness arise from changes in the intrinsic mobility of the dislocations, the mobile dislocation density, and/or from dislocation generation and distribution at crack tip interactions which delay the brittle fracture process.

More recently, Levit et al. [19] showed that it is possible to achieve a high tensile elongation of ~25% by optimizing factors such as impurity content, heat treatment, orientation, prestraining and surface condition of NiAl single crystals. In their experiments, homogenized high purity, stoichiometric single crystals were prestrained (compressed) at 1273 K before undergoing tensile test under ambient conditions. These high temperature prestraining leads to an increase in the tensile elongation from an average of 16% to 26%. The authors concluded that the high temperature prestraining resulted in the production of a

dislocation-free subgrain volumes, separated by low energy dislocation boundaries. These subgrain volumes act as a source for mobile dislocations.

These recent studies have lead to the proposition that NiAl and BCC metals having levels of interstitial impurities, are subject to a strain aging phenomenon caused by elastic interactions between the interstitial atoms and dislocations.

The term strain aging indicates a time-dependent strengthening or hardening process resulting from elastic interaction of solute atoms with the strain fields of dislocations in plastically deformed metals and alloys [20]. Aging reactions can occur in either static or dynamic modes depending upon whether they occur prior to or during plastic deformation. As discussed by Weaver [21], static strain aging typically occurs in metals and alloys following prestraining, unloading (either partially or fully), aging for a prescribed time and then reloading at the same strain rate as the prestrain. It is typically manifested by an increase in yield stress or flow stress following aging and the return of a sharp yield point in the deformed alloy. Dynamic strain aging, the result of interactions between diffusing solute atoms and mobile dislocations during plastic deformation, is manifested by the appearance of serrations, load drops, jerkiness or other discontinuities in the stress-strain curves obtained in constant-extension-rate tensile or compression tests. These phenomena are associated with the dynamic formation and migration of solute atmospheres around dislocations during deformation.

The brittle fracture of structural materials have also been studied using in-situ straining TEM. Many authors [22-24] have used in-situ straining TEM to observe dislocations near the crack tips in the hope of characterizing the role of dislocations at the crack tip regions and how the crack tip stress field can be modified by these dislocations.

The limitation of these studies is the constraints imposed by the requisite thin foils. This present study uses electron channeling contrast imaging (ECCI) to image dislocations at the crack tips of bulk specimens. This technique has gain attention as a potential method for imaging near surface crystal defects of bulk specimens and will be describe in detail in chapter 3. In order to explain the significance of the ECCI studies, a a brief review of crack tip deformation and its impact on the dislocation theory of fracture is useful.

In general, dislocations are emitted from the crack tips during the early stages of crack propagation and are driven out of the crack tip area, leaving behind a dislocation-free zone (DFZ) (Figure 4). In metals with low stacking fault energies the dislocations pile up in the form of linear arrays on a slip plane which is coplanar with the crack. In metals with high stacking fault energies, the dislocations cross slip out of the original slip planes and form a broad plastic zone. The cracks propagate by a combination of plastic and elastic processes in which the plastic portion of the crack opening is created by the dislocations that were emitted from the crack tip while the elastic process occurs as a result of brittle fracture of the dislocation-free zone (DFZ) along the slip planes. After emitting a number of dislocations, the crack propagates along the slip planes of these dislocations. As the crack propagates, the

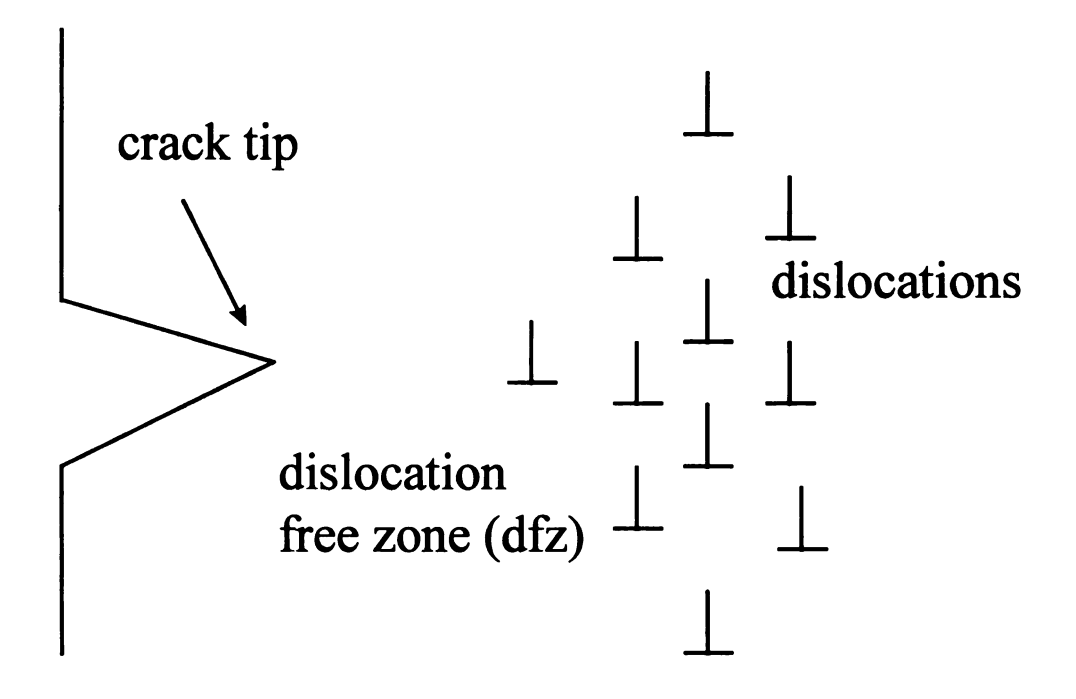


Figure 4. Cracks propagate by a combination of plastic and elastic process. Plastic portion of the crack is created by the dislocations. Elastic portion of the crack is a result of brittle fracture of the dfz

When a dislocation is emitted from a crack tip, it exerts a back stress to the crack tip thus reducing the local stress intensity factor k (Figure 5). This phenomenon is known as the dislocation shielding of the crack tip [25,26]. Figure 6 shows a schematic diagram of a crack, the dislocation free zone and plastic zone in an infinite elastic medium. As mentioned by Chang and Ohr [22], if the applied stress is fixed, the increase of the total number of dislocations, which is essentially equal to the crack opening displacement (COD), corresponds to a decrease of the length of the DFZ (e/c) and an increase of the length of the plastic zone (a/c).

where COD= $(4c\sigma/\pi\mu) \ln(a/c)$,

and σ = friction stress in the plastic zone

 μ = shear modulus

a = length of the plastic zone

2c= length of crack

e = length of DFZ

Thus the stress relaxation can be viewed as a result of an increase in the total number of dislocations within the plastic zone. The local k is very sensitive to the length of the DFZ [22,23]. When the DFZ is absent, the shielding of the crack tip by the dislocations is complete and hence the local k is reduced to zero. In this situation, no thermodynamic driving force exists for this crack to propagate. For a complete review of the crack tip deformation and its impact on the dislocation theory fracture, see ref. 22-24.

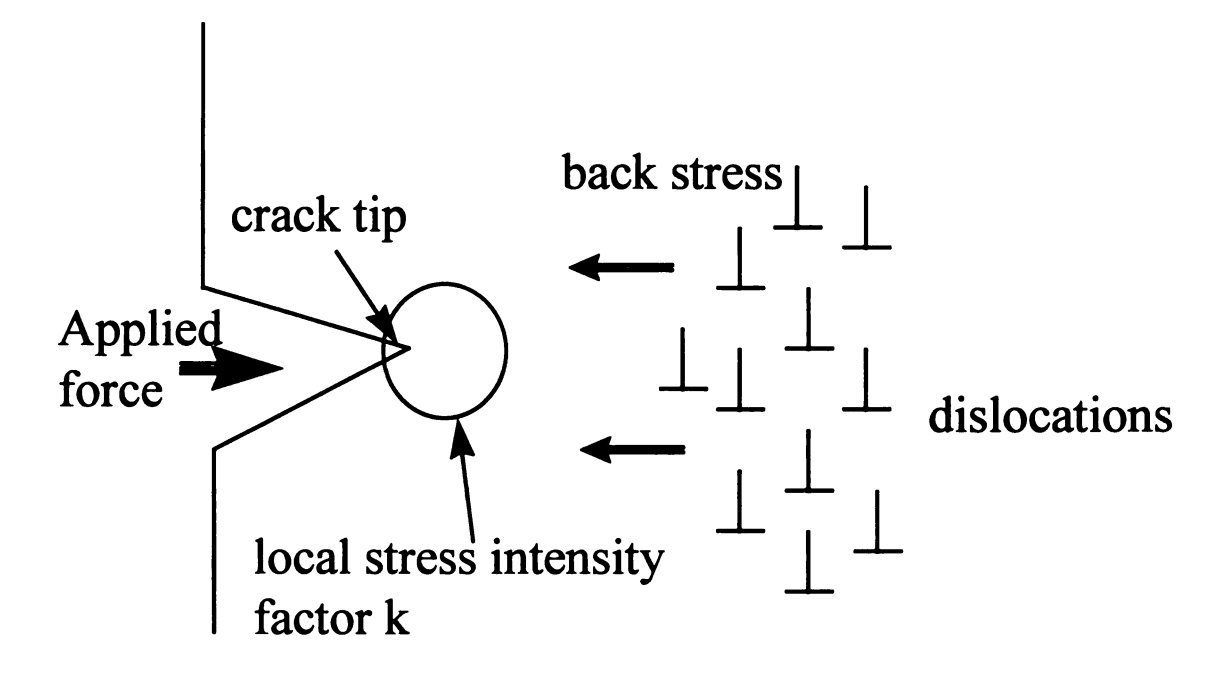


Figure 5. The emitted dislocations exert a back stress to the crack tip thus reducing the local stress intensity factor k. Stress relaxation is viewed as a result of an increase of the total number of dislocations within the plastic zone.

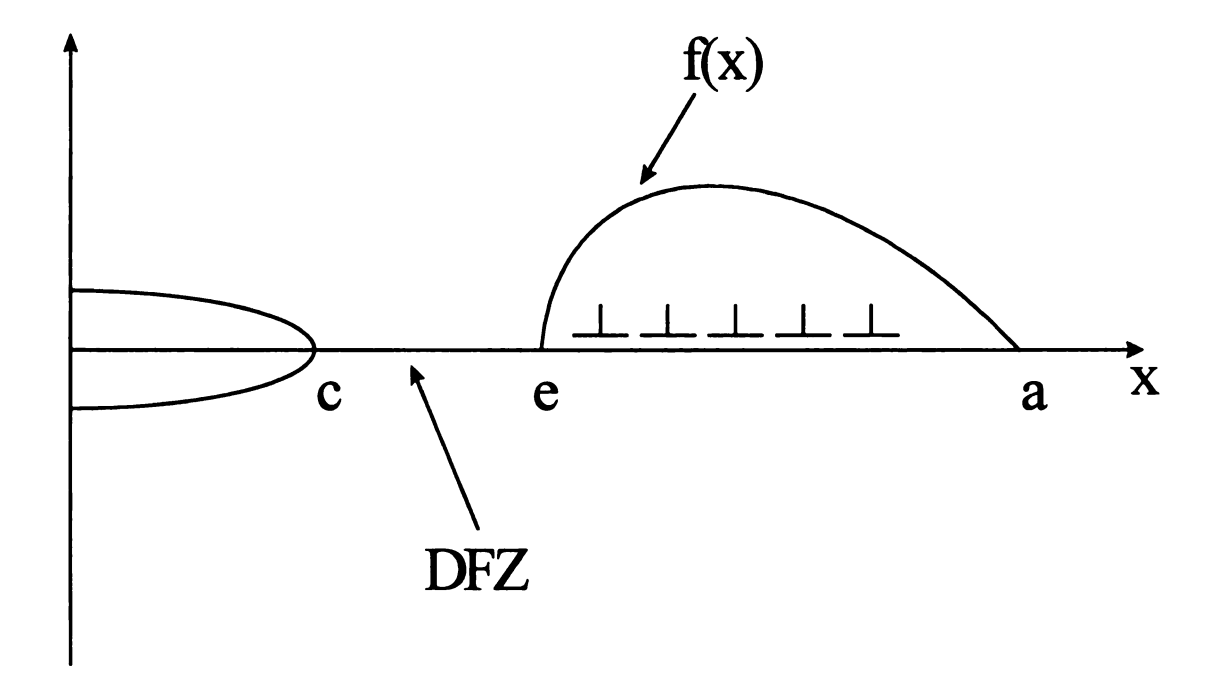


Figure 6. Crack, the dislocation free zone and plastic zone in an infinite elastic medium. f(x) is the distribution function of the dislocations. Adapted from [22].

Slip Systems in NiAl

Critical to understanding the mechanical behavior of any material is the study of the dislocations and slip systems of the material.

In general, <100> dislocations are the most commonly observed dislocations in deformed NiAl single crystals [19,27-30]. These <100> dislocations have been observed to slip on both {011} and {001} planes. The critical resolved shear stress (CRSS) calculation based on 0.2% yield stress, for slip on the <100> {011} and <100>{001} systems, are similar [31] and results in the active slip plane being a function of single crystal orientation.

While <100> dislocations are the most commonly observed dislocations in deformed NiAl, <111> dislocations have also received considerable attention. This is due to the expectation that activation of the <111> slip might result in enhanced ductility in polycrystal NiAl as <111> slip is capable of satisfying the Von Mises criteria of five independent slip systems. Based on this premise, many current research efforts have been concentrated on encouraging slip of the <111> type. These <111> dislocations have been activated in single crystals by some researchers [32,33] by inhibiting the slip of <100> dislocations. Slip of <100> dislocations may be inhibited by orienting to the <001> "hard" orientation where the resolved shear stress in the <100> slip direction is very low and only at or below room temperature. <111> slip has also been achieved by alloying with Cr and Mn [34,35]. However it should be noted that the generation of <111> dislocations has never resulted in increased plasticity [34].

<110> dislocations have been observed for deformation temperatures above 873 K [32,35,36]. Like <111> dislocations at lower temperature, these <110> dislocations can only be produced by inhibiting the slip of <100> dislocations by orienting single crystals to <001>

hard orientations. At present there is still some questions as to what extent these <110> dislocations contribute to plastic strain. Fraser et al. [37] have argued that these <110> dislocations, the products of the interaction of two <100> dislocations, are sessile and do not contribute to the plasticity of NiAl. Field et al.[31] on the other hand showed that <110> dislocations are actually responsible for plasticity and that <100> dislocations are debris resulting from a slip dissociation of <110> screws at superjog and that it is primary the debris that is being observed, and not the actual slipping dislocations.

1.4 Observations of dislocations in enhanced plasticity NiAl

As outlined in the section on dislocations above, there has been some success in enhancing the ambient temperature ductility and toughness of NiAl. These studies have used microalloying, controlled thermal treatment and prestressing to presumably increase dislocation mobility and/or generation. However, these studies have been complimented with only limited observations of the dislocation structures associated with enhanced plasticity.

Standard diffraction contrast (g.b) experiments carried out by Levit et al. [19] revealed that essentially all the dislocations had <100> Burgers vectors.

In the case of improved tensile elongation as a result of microalloying, weak beam TEM analysis revealed no differences between alloyed materials and binary materials tested in compression [18]. In both cases, similar structures, dominated by <100> dislocations were observed. The dislocations produced as a result of hydrostatic prestress were also reported to be <100> type dislocations [14,15]. However, the analysis presented in the study is not entirely clear.

With regards to the strain age phenomenon reported by Hack's group [8,9], analysis of the dislocation structures has not been performed.

1.5 Objectives

It is the objective of this study to examine the types of dislocations, their behavior, as well as the dislocation distribution in the region of the crack tips and crack edges of both toughened and embrittled single crystal NiAl. This has been carried out using the transmission electron microscopy (TEM) as well as scanning electron microscopy (SEM).

Since no dislocation structures were analyzed in Hack et al.'s [8,9] studies, this study examined the role of dislocations and how it affects static strain aging in the brittle behavior of NiAl. The heat treatment processes as outlined by Hack et al.'s [8,9] for toughened and embrittled conditions of single crystal NiAl were used in order to duplicate similar conditions as reported in their studies. After heat treatment, selected specimens were subjected to room temperature compression to 2.5% plastic strain to induce dislocation generation. These deformed specimens have been prepared for examination in the TEM. The results have been compared to undeformed specimens. Other specimens have been examined employing the electron channeling contrast imaging (ECCI) technique performed using SEM to observe dislocation behavior and generation in 4-point bend specimens in the region of crack tips.

CHAPTER 2

TEM EXAMINATION

2.1 Experimental Procedure

Commercial purity stoichiometric single crystal NiAl was oriented by xray diffraction using the back-reflection Laue technique to lie within the stereographic triangle as shown in Figure 7. Specimens measuring 4.5x4.5x10 mm were cut using a high speed diamond blade wafering saw. In order to duplicate the embrittled and toughened conditions as reported by Hack et al. [8,9], these specimens were then given a homogenization anneal at 1590 K for 48 hours in a Centorr Vacuum Furnace followed by either furnace cooling with a cooling rate of ~0.1 K/s (specimens denoted as 1590FC) or air cooling, with a cooling rate of ~ 1 K/s. Samples that were air-cooled were reheated to 1573 K in the same furnace for 3 hours and air cooled (1590AC). Some of these 1590AC were then reheated to 473 K for 90 minutes and furnace cooled (473FC). Samples (1590FC) that were furnace cooled after the initial homogenized anneal were reheated to 673 K in a Lindberg furnace for 12 hours and were either air-cooled (673AC) or furnace cooled (673FC). The embrittled specimens are 1590FC, 473FC and 673FC whereas the toughened specimens are 673AC and 1590AC. The flow chart of the various heat treatment processes is shown in Figure 8.

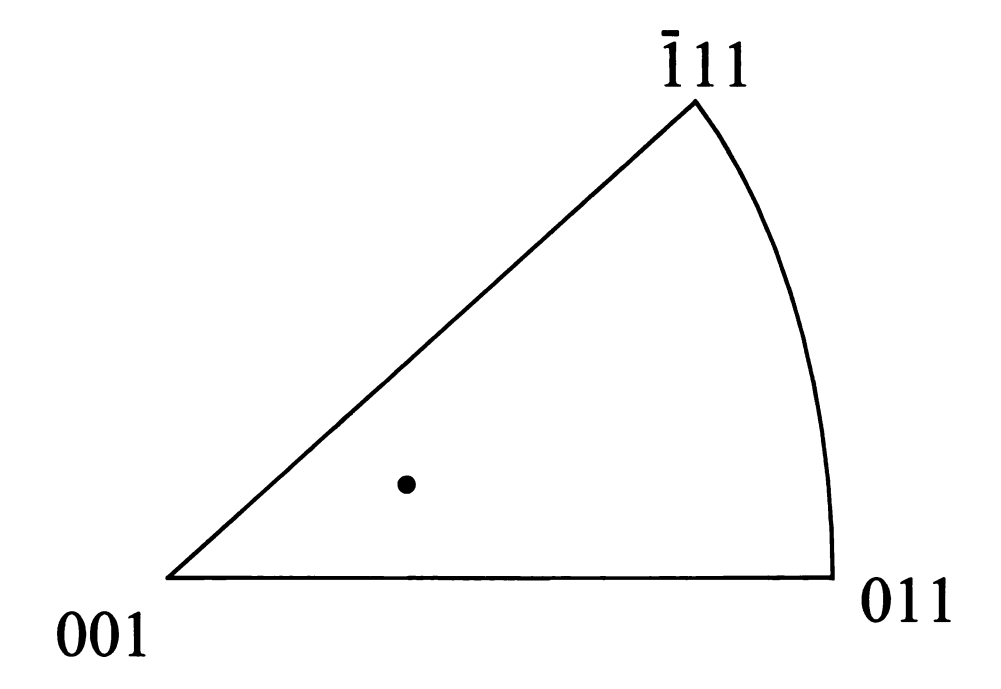


Figure 7. Orientation of specimen within the stereographic triangle.

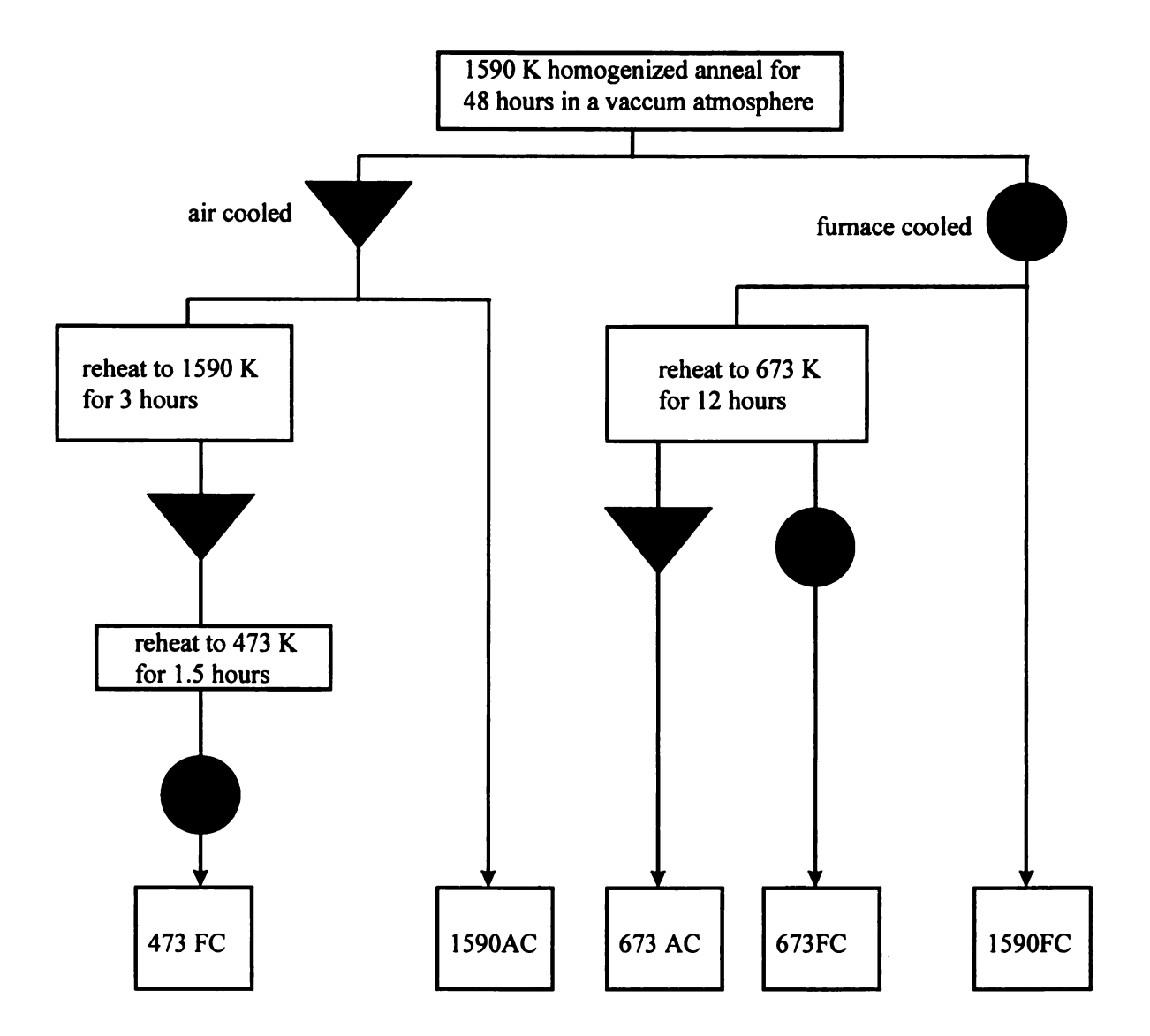


Figure 8. Flow chart of the heat treatment procedure. Adapted from [8,9].

Some of these heat treated samples were then mechanically ground and polished to 0.3 µm using Al₂O₃ polishing medium. These polished specimens were then placed in a compression fixture and subjected to room temperature compression using an Instron Machine model 4206. These samples were compressed at a nominal strain rate of 10⁻⁴ per second to 2.5% plastic strain to induce dislocation generation and slip. Using optical microscopy, the slip lines were observed and the active slip planes were determined by standard slip trace analysis which will be explained in section 2.2.

Undeformed and deformed samples were then cut into 3 mm diameter rods and sectioned parallel to the slip planes using electro-spark machining. These discs were then ground to 0.3 mm using grit SiC paper and electropolished using a twin-jet polisher. The electrolyte consisted o one part nitric acid (HNO₃) to three parts methanol. Electropolishing was performed at a temperature of 243 K and a voltage of 12 V. Dislocation observation was performed using a H-800 Hitachi TEM. Burger's vectors of the dislocations were determined using the standard g•b=0 invisibility criteria.

2.2 Slip Trace Analysis

Following compression, the specimens were examined optically to observe dislocation slip traces. An example of slip traces on two perpendicular faces is shown in Figure 9. The active slip planes were determined by trace analysis. An example of which is given as follows. The angles α and β were measured on a pair of micrographs showing the front and right faces of the rectangular compression sample as shown in Figure 10.

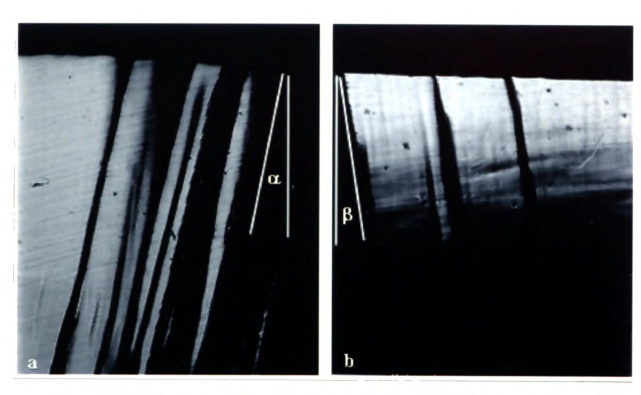


Figure 9. Two faces of a deformed specimen showing the slip planes with measured angles α and $\beta.$

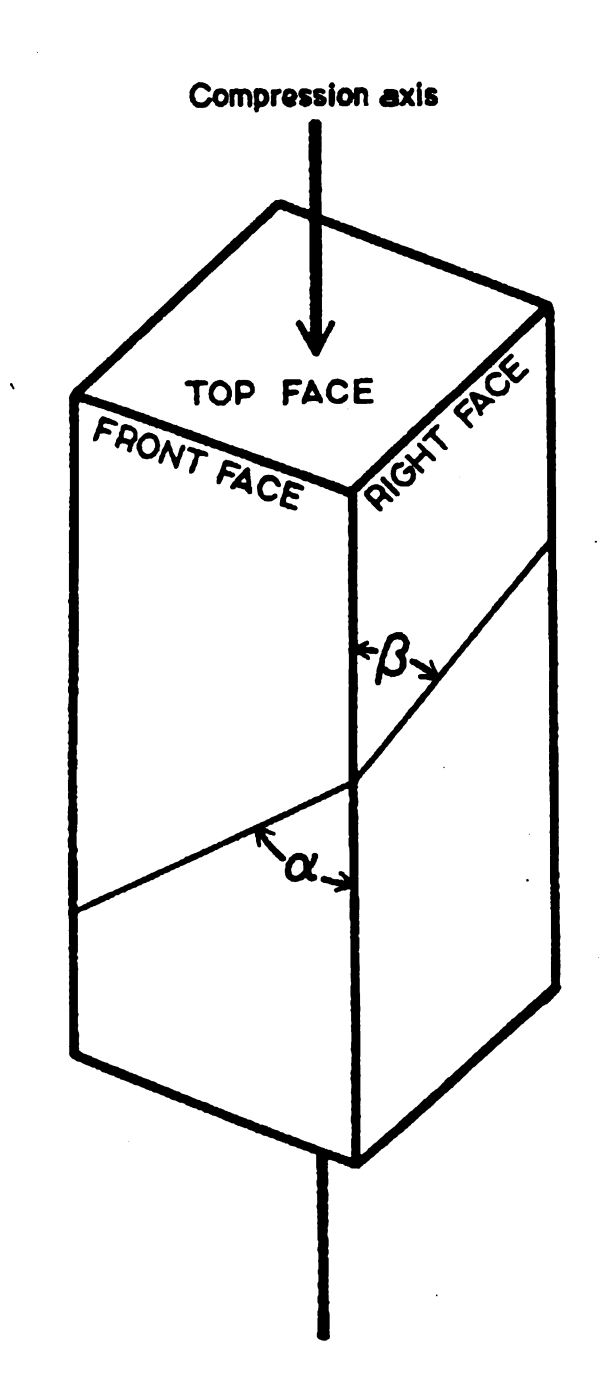


Figure 10. Schematic representation of a compression sample displaying the measurement of α and β used in determining the slip plane.

The angles were then plotted on the stereographic projection of the front face in the manner shown in Figure 11. The two angles define the plane which causes the slip trace on the single crystal. The plane and its pole (90 degree from the plane) are shown on the stereographic projection. In all cases, regardless of heat treatment and cooling rates, {100} was analyzed as the slip plane.

2.3 Dislocation analysis

Dislocation observation and analysis was performed on a Hitachi H-800 200KV transmission electron microscope using the brightfield as well as weak beam imaging. To obtain a sufficient number of **g** vectors for contrast analysis, the primary poles, {001}, {011} and {111} were used. As NiAl is an anisotropic crystal, the dislocations may not be completely invisible when **g**•**b**=0 and **g**•**b**x**u**=0 conditions are satisfied [38]. This is because no planes remain undistorted around edge or screw dislocations because of the anisotropy. Thus the invisibility method for determining **b** often relies on finding diffraction vectors which result in weak contrast rather than complete invisibility. Computer simulation was used where possible, to confirm the Burger's vectors. This will be described in section 2.5.

2.4 Results

Data obtained from the compression tests are shown in Table 1. These show the yield strength of each specimen tested, along fracture toughness values from Hack et al.

[8,9] corresponding to the same heat treatments. It is observed that a slow cooling rate (furnace cooled) tends to increase the yield strength but correspondingly results in lower

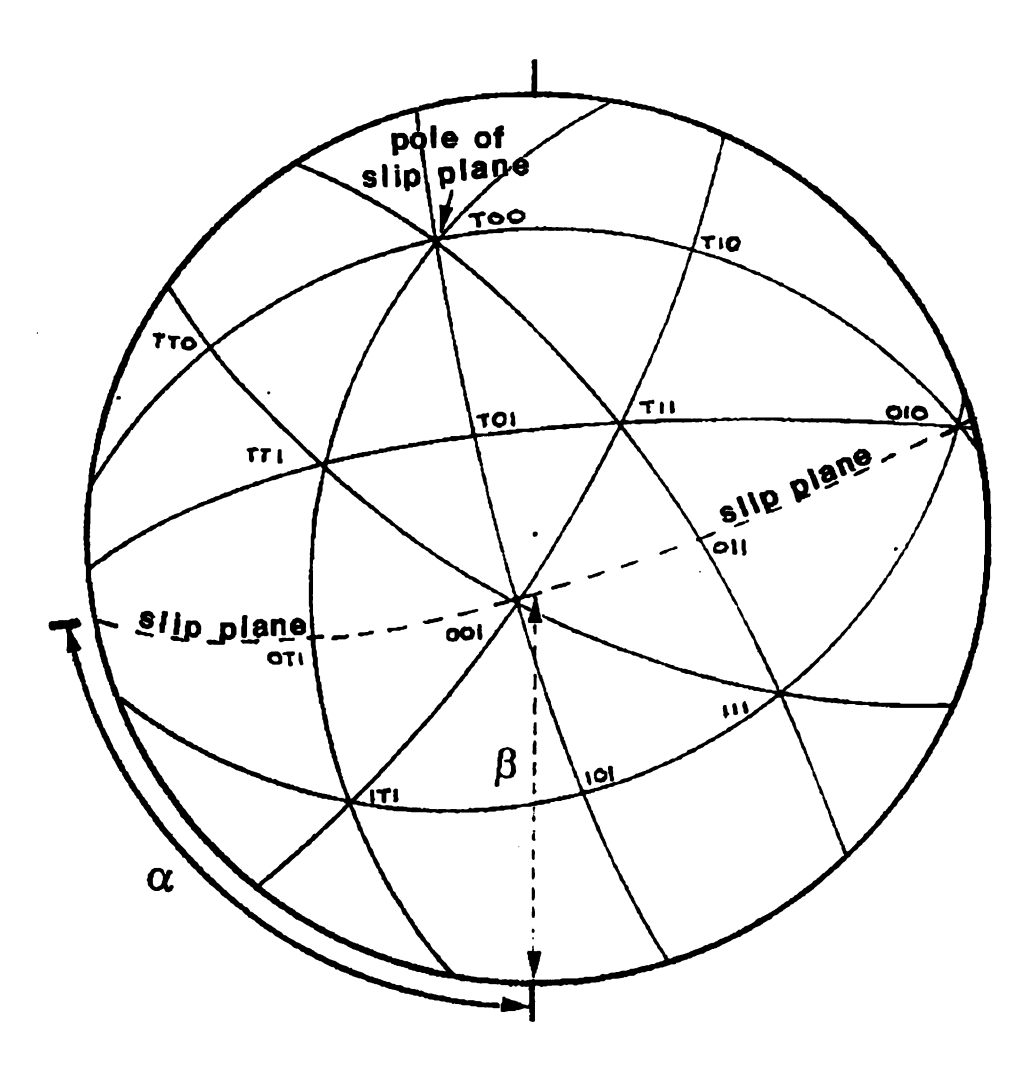


Figure 11. Sterographic projection of the specimen displaying the angles α and β used to determine the slip plane.

Table 1. Properties of test specimens

Specimen	Condition of specimen	Yield	*Fracture
Specimen	Condition of specimen		
		Stress	Toughness
		MPa	MPa.m ^{1/2}
473FC	1590 K homogenization anneal and air	400	2.8
	cooled. Reheated to 1573 K and air cooled.		
	Then reheated to 473 K and furnace cooled.		
1590FC	1590 K homogenization anneal and furnace	450	2.4/4.0
	cooled.		
673FC	1590 K homogenization anneal and furnace	360	5.8
	cooled. Reheated to 673 K and furnace cooled.		
1590AC	1590 K homogenization anneal and air cooled.	260	15.6
673AC	1590 K homogenization anneal and furnace cooled. Reheated to 673 K and air cooled.	150	16.7

^{*}Adapted from Hack et al. [8,9]

fracture toughness, whereas fast cooling (air cooled) tends to decrease the yield strength but results in a much higher fracture toughness value. The dislocation structures of each specimen were examined and the Burgers vectors **b** were determined using the **g·b=0** invisibility criterion. Generally dislocations will be invisible when their **b** lies in the reflecting plane. Using two-beam conditions for a series of individual reflections, two such conditions of invisibility should be found. As **b** is common to both reflections, **b** must be the zone axis of the two planes.

2.4.1 Undeformed Specimens

Burgers vector characterization of an undeformed 673FC specimen is shown in fig. 12. The "a" dislocations with $\mathbf{b} = [0\ 0\ 1]$ are observed to be in weak contrast for both $[2\ 0\ 0]$ and $[1\ 1\ 0]$ reflections while the "b" dislocations $\mathbf{b} = [0\ \overline{1}\ 1]$ are observed to be in weak contrast in both $[2\ 0\ 0]$ and $[0\ 1\ 1]$ reflections.

Figure 13 shows micrographs of undeformed 473FC and 673AC specimens exhibiting <001> and <011> dislocations. Likewise, undeformed 1590AC and 1590FC specimens show similar types of dislocations. It is noted that majority of the dislocations displayed in all the undeformed specimens are dominantly <001> type with a few scattered <011> dislocations.

The gross morphologies of all the undeformed specimens show similar dislocation densities. Figure 14 shows micrographs of 473FC, 673FC and 673AC specimens showing single dislocations widely spaced with few dislocation loops and tangles.

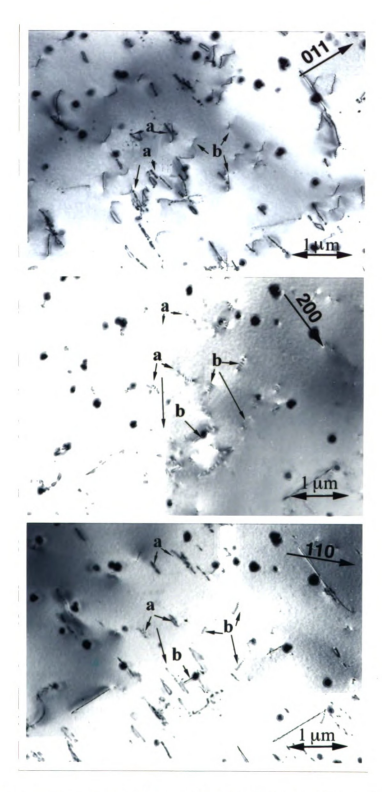


Figure 12. Burgers vector analysis for undeformed 673FC specimen. The same area is shown with different operative reflections: [011], [200] and [110]. 'a' denotes <001> and 'b' denotes <011>.

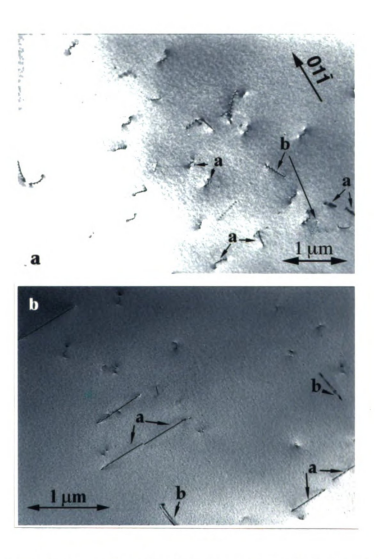


Figure 13. Micrographs of a) 473FC specimen and b) 673AC specimen displaying both <001> and <011> dislocations. 'a' denotes <001> and 'b' denotes <011>.

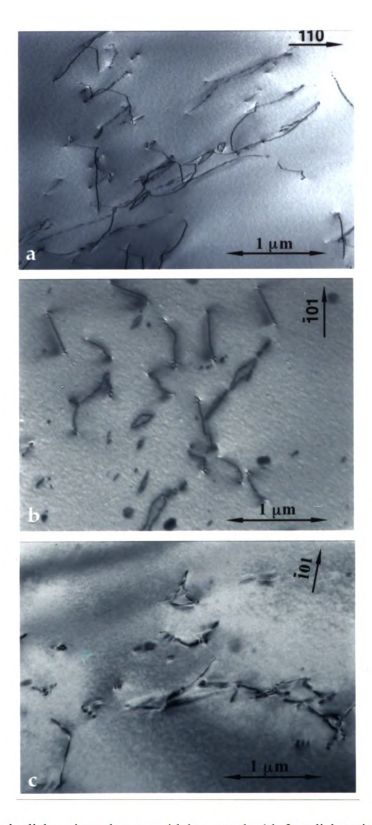


Figure 14. Single dislocations that are widely spaced with few dislocation loops and tangles were observed in a) undeformed 473FC specimen, b) undeformed 673FC specimen and c) undeformed 673AC specimen.

2.4.2 Deformed Specimens

Figure 15 shows a Burgers vector analysis for a deformed 673AC specimen, which posses a low yield stress value of 150MPa. The "b" dislocations $\mathbf{b} = [\ 0 \ 1 \ \overline{1} \]$ are observed to be in complete extinction in the $[\ 2 \ 0 \ 0 \]$ reflection and weak in $[\ 2 \ \overline{1} \ \overline{1} \]$ reflection. The "a" dislocations are analyzed as $\mathbf{b} = [\ 1 \ 0 \ 0 \]$ which displays extinction/weak contrast in both $[\ 0 \ \overline{2} \ 0 \]$ and $[\ 0 \ \overline{1} \ 1 \]$.

The deformed 673FC specimen, which possess a higher yield stress (300MPa.) than the 673AC specimen, is shown in Figure 16. Burgers vector analysis show that dislocations with $\mathbf{b} = [\overline{1} \ 0 \ 0]$ are observed to be in extinction for $[0\ 1\ \overline{1}]$ reflection and in weak contrast for $[0\ 2\ 0]$ reflection whereas dislocations with $\mathbf{b} = [0\ 1\ \overline{1}]$ are observed to be in weak contrast for both $[\overline{2}\ 0\ 0]$ and $[\overline{2}\ 1\ 1]$ reflections.

Deformed 473FC, 1590FC, and 1590AC specimens were also analyzed as having both < 0.01 > and < 0.11 > dislocations (see Figures 17-19 respectively).

Based on these observations, regardless of heat treatment, cooling rates, and corresponding yield strength, it has been determined that the dislocations exhibit similar Burgers vectors, i.e. < 0 0 1 > and < 0 1 1 >, although primarily <001> dislocations with scattered <011> dislocations. Dislocations were observed to move under the influence of the electron beam indicating that although these materials do not display extensive ductility, the dislocations in the structures are mobile. Table 2 summarized Burgers vectors analyzed for each of the tested specimens in relation to their heat treatment histories and yield strength.

The gross morphology of each of the specimens was examined to determine the type of dislocation structures present. Using both bright field and weak beam imaging it

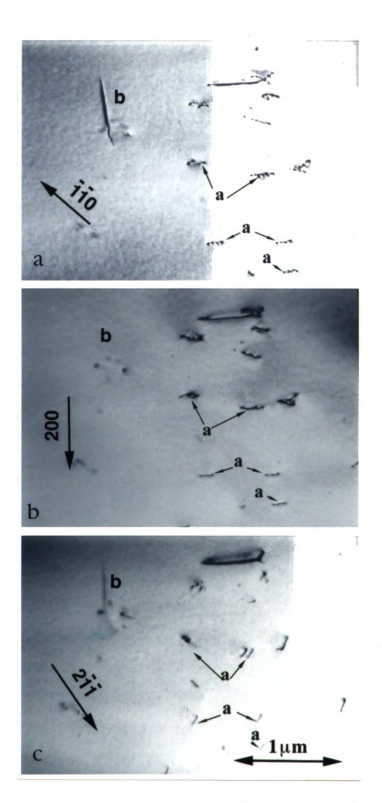


Figure 15. Burgers vector analysis for deformed 673AC specimen shows both "a" The same region with $\mathbf{b} = [1\ 0\ 0]$ and "b" dislocations with $\mathbf{b} = [0\ 1\ \overline{1}]$ present. The same region with different operative reflections are shown: a) $[\overline{1}\ \overline{1}\ 0]$, b) $[2\ 0\ 0]$, c) $[2\ \overline{1}\ \overline{1}]$.

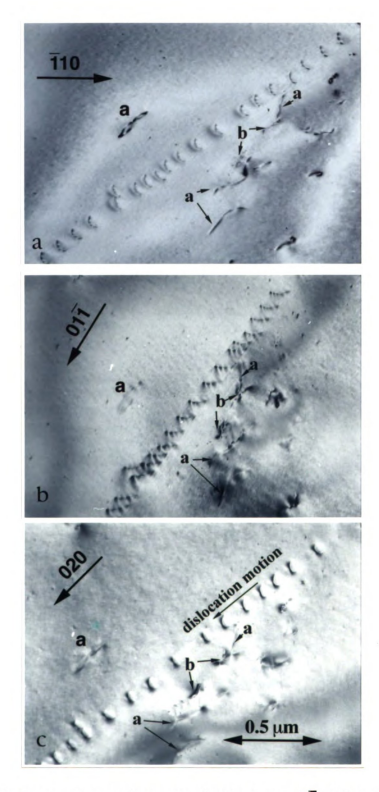


Figure 16. Burgers vector analysis revealed both $\mathbf{b} = [\ \overline{1}\ 0\ 0\]$ and $\mathbf{b} = [\ 0\ 1\ \overline{1}\]$ dislocations present in deformed 673FC specimen. The same area is shown with different operative reflections a) $[\ \overline{1}\ 1\ 0\]$, b) $[\ 0\ 1\ \overline{1}\]$, c) $[\ 0\ 2\ 0\]$.

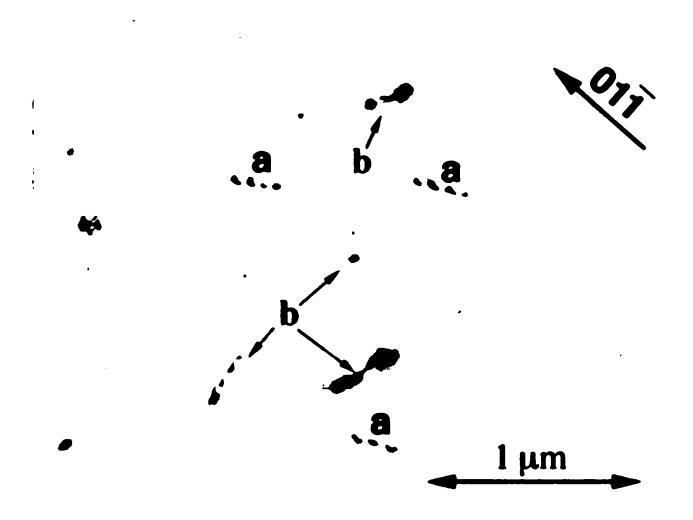


Figure 17. Micrographs of deformed 473FC specimen displaying both <001> and <011> dislocations. 'a' denotes <001> and 'b' denotes <011>.

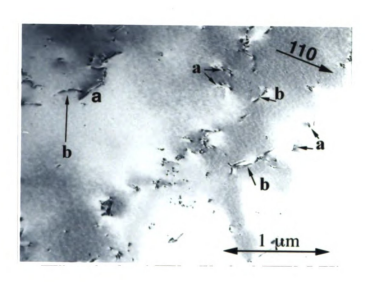


Figure 18. <001> and <011> dislocations were observed in deformed 1590FC specimen. 'a' denotes <001> and 'b' denotes <011>.

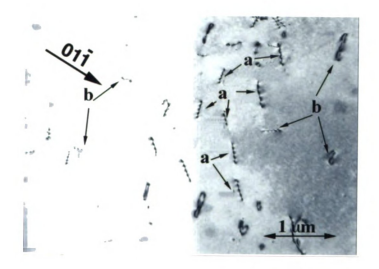


Figure 19. Burgers vector analysis reveals both <001> and <011> dislocations present in deformed 1590AC specimen. 'a' denotes <001> and 'b' denotes <011>.

Table 2. Burgers vectors analyzed for each of the tested specimens in correlation to their heat treatment histories and yield strength.

Specimens	Yield Stress MPa	Burgers vector b	
473FC	400	Primarily <001>	Scattered <011>
1590FC	450	Primarily <001>	Scattered <011>
673FC	360	Primarily <001>	Scattered <011>
1590AC	200	Primarily <001> Scattered <0	
673AC	150	Primarily <001>	Scattered <011>

was observed that deformed 473FC and 1590FC specimens, having the highest yield strength compared to the rest of the samples, show dislocations that are heavily tangled (Figures 20 and 21 respectively). Dislocations, which moved under the influence of the electron beam, were observed to be restrained when they moved into these tangles. These dislocation tangles thus appear to act as obstacles to dislocation motion. The 673FC specimen, displaying fewer dislocation tangles as compared to both 473FC and 1590FC specimens, is shown in Figure 22. 1590AC specimen (Figure 23) and 673AC specimen (Figure 24), which were toughened and displayed lower yield strengths, were observed to have very few dislocation tangles and as such, dislocations were able to move without many obstructions.

From this examination, it is concluded that deformed specimens having higher yield stresses (and hence lower fracture toughness) tend to have dislocations that are heavily tangled, whereas specimens having lower yield strengths (and hence higher toughness) tend to have fewer dislocation tangles. These dislocation tangles are a result of deformation following the compression tests as undeformed specimens do not display dislocations that are heavily tangled. Deformed specimens displaying heavily tangled dislocations had undergone furnace cooling. On the other hand, deformed specimens which do not show much dislocation tangles had been rapidly cooled. This leads to the possibility that with slow cooling, there is sufficient time for interstitial to positions at or near the cores of dislocations and results in strain aging embrittlement [13]. Such behavior is consistent with static strain aging reported by Weaver [21] who concluded

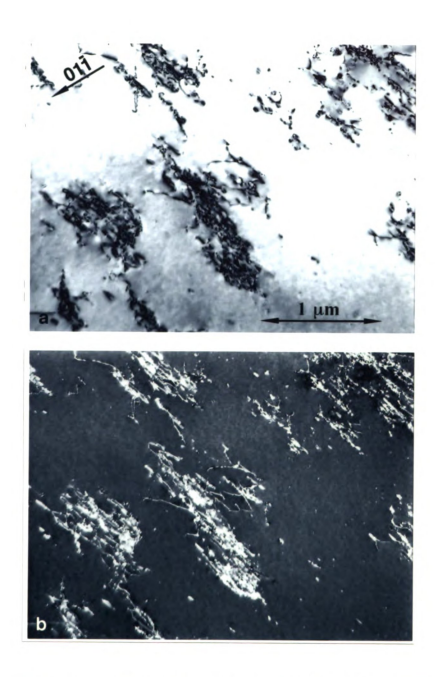


Figure 20. Dislocations were observed to be heavily tangled in deformed 473FC specimen. a) brightfield image and b) weak beam image.

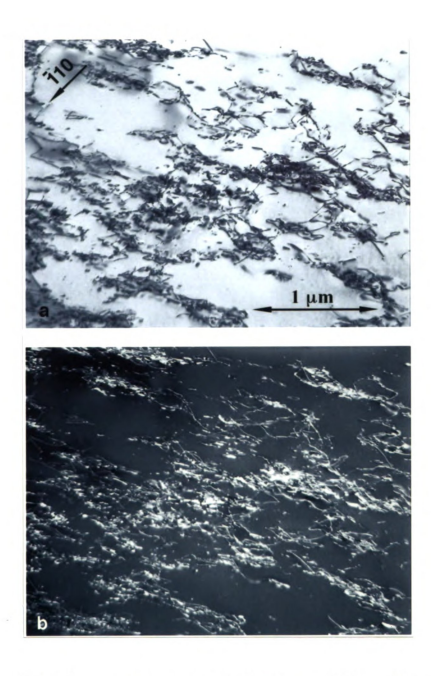


Figure 21. Dislocations were observed to be heavily tangled in deformed 1590FC specimen. a) brightfield image and b) weak beam image.

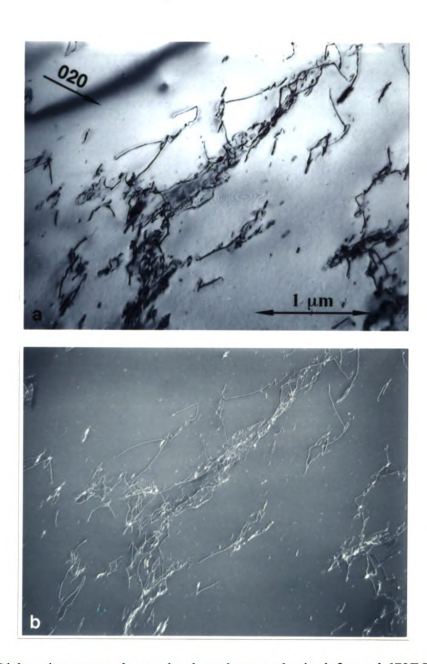


Figure 22. Dislocations were observed to have less tangles in deformed 673FC specimen. a) brightfield image and b) weak beam image.

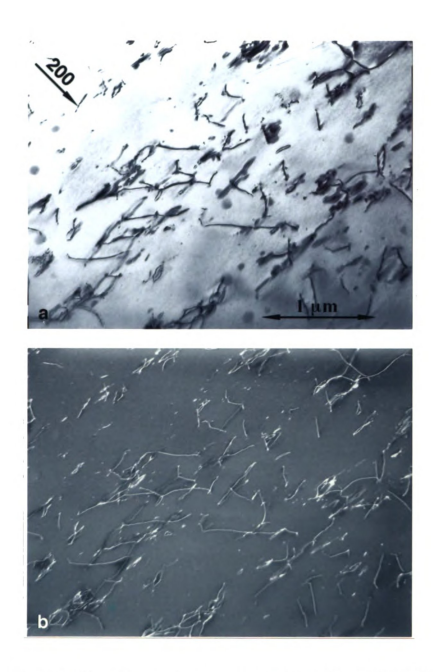


Figure 23. Very few dislocation tangles were observed in deformed 1590AC specimen. a) brightfield image and b) weak beam image.

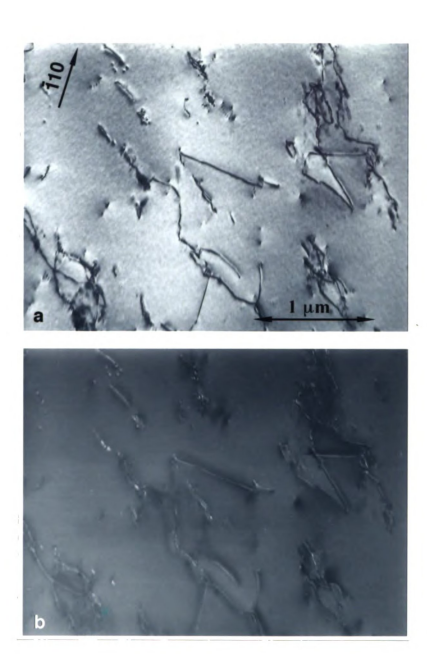


Figure 24. Very few dislocation tangles were observed in deformed 673AC specimen. a) brightfield image and b) weak beam image.

that it is the interstitial C that is responsible for yield stress obtained for furnace cooled specimens. Fast cooling on the other hand would 'trap' the interstitials in the solution. As a result the pre-existing dislocations are not pinned and so more mobile dislocations are available. This would result in the lower yield stress obtained for air-cooled specimens. High yield stress (or low fracture toughness or a lack of ductility) then must have derive from the low mobility of dislocations.

The observation of heavily tangled dislocations in deformed specimens that are furnace cooled (slow cooling) have led to the conclusion that static strain aging occurs as a result of having sufficient time for the interstitial to diffuse into the cores of dislocations and pinning them. Hence these observations support Hack et al.'s [8,9] conclusion that the brittle behavior in single crystal NiAl were a result of a static strain aging induced reduction in mobile dislocation density.

2.5 Computer Simulation

The use of experimentally invisible or weak images to detect diffracting conditions in which $\mathbf{g} \cdot \mathbf{b} = 0$ is open to the criticism that dislocations in elastically anisotropic materials often display residual contrast. On the other hand, the invisibility criteria is simple to use and there seems to be no doubt that in the majority of cases examined, experimental invisibility coincide with $\mathbf{g} \cdot \mathbf{b} = 0$. As most materials are usually anisotropic and dislocations are in general neither of screw nor edge orientation, true invisibility can be difficult to achieve experimentally. For this reason, an image matching technique is sometimes used to confirm Burgers vectors. This technique is based on computer simulation of a series of dislocation images and matching these simulated

images with experimental images. The computer program used in the present study, which was adapted from Head et al. [39], is based on the dynamical theory of image contrast.

The general method of identification of defects using the computed micrographs may be stated as follows; experimental micrographs of the unknown defects are taken under different diffracting conditions, e.g. different diffracting vectors taken in different electron beam directions. Then informed guesses are made as to what the unknown defect might be and theoretical micrographs are computed for these under the same diffracting conditions as the experimental micrographs. When the theoretical and experimental micrographs match consistently, the defect is identified.

Unlike the use of invisibility criteria, this technique of computerized image matching does not involve only the choice of weak or invisible images. On the contrary, the images which are well suited to the comparison technique are often those which have easily distinguished topological features; that is, images with 'character'.

In order to obtain the data necessary for accurate simulation, micrographs and their corresponding diffracting patterns should be collected in such a way that the crystallography of the defect and of the foil, as well as the diffracting conditions for each micrograph, can be specified as completely as possible. The procedure for obtaining this experimental information involves taking, for the same defect, a series of electron micrographs and corresponding selected area diffraction patterns for a number of different beam directions and diffracting conditions. It is important to recognize the kikuchi line patterns associated with low index crystallographic directions for the material under consideration. Important data includes the operative diffracting vector \mathbf{g}

for each micrograph, the beam direction **B**, the dislocation line direction **u**, the foil normal **F**, a value of the deviation from the Bragg condition **w**, the foil thickness **t**, and the anomalous absorption coefficient. Methods of obtaining the above parameters are given in ref. [39].

The first step in determining a Burgers vector by image computation involves choosing a set of experimental images of the dislocation from the available micrographs. Figure 25 shows a dislocation marked 'A' in an undeformed 673AC specimen. This dislocation image will be used to illustrate the technique of defect identification by image matching. It should be noted that the matching progress will be greatly facilitated if the images have distinctly differing topologies arising from distinguishing features of contrast. Moreover, the chosen set should contain three non-coplanar diffracting vectors in order to sample all components of the displacement field of the defect.

A set of micrographs of dislocation 'A' are shown in the first column of Figure 26 and labeled (a) - (g). The diffracting vectors **g**, beam directions **B** and values of the deviation from the Bragg condition **w**, corresponding to each micrograph are listed in Table 3 together with the appropriate values of theoretical two-beam extinction distances and the values of apparent anomalous absorption coefficient. In addition to the set of seven experimental images, four corresponding sets of computed images for different possible Burgers vectors are presented. These images have been computed for the diffracting conditions specified by the values given in Table 3. The object is to select the set of computed images that is in best visual agreement with the experimental set. As shown, the computed images for Burgers vector [1 0 0] and ½ [1 1 0] are not in agreement with the experimental image (c) and the computed images with Burgers vector

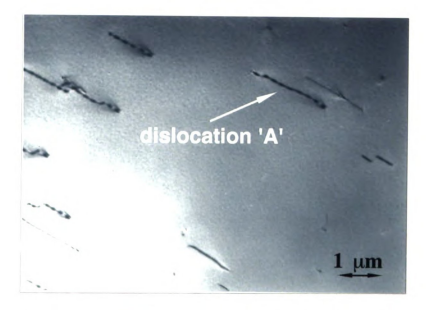


Figure 25. Dislocation marked 'A' in an undeformed 673AC specimen which will be used to illustrate the technique of defect identification by image matching.

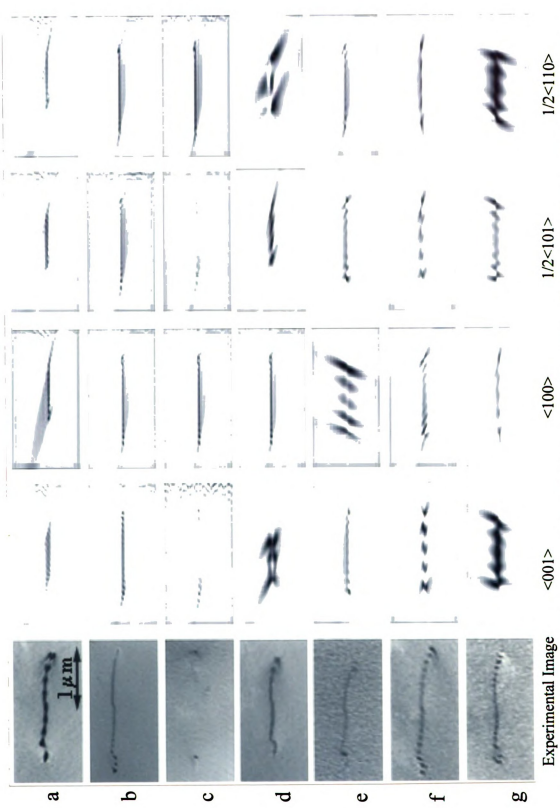


Figure 26. A set of experiment images (a) - (g) of dislocation 'A' taken with the diffraction conditions given in Table 3 and four sets of computed images for the same diffraction conditions coresponding to the Burgers vectors shown.

Table 3. Parameters used in simulating dislocation 'A'

g vector	<u>2</u> 00	110	020	<u>2</u> 00	0 1 1	<u>1</u> 10	0 1 1
LU	5 23 6	5 23 6	5 23 6	5 23 6	<u>5</u> 23 6	5 23 6	5 23 6
LBM	016	<u>2</u> 2 15	4 0 19	0911	<u>1</u> 33	<u>1</u> 5 1 5	4 99
LFN	1112	<u>1</u> 112	1112	<u>1</u> 112	<u>1</u> 112	<u>1</u> 112	<u>1</u> 112
w	0.8	0.85	0.6	0.4	0.7	0.6	0.26
t	1.3	3.5	4	1.3	3	3	2.16

where

LU = direction of dislocation line

LBM = electron beam direction

LFN = foil normal

w = deviation from Bragg condition

t = foil thickness in extinction distances

Other parameters used include:

Elastic constants: C11 = 2.03 C12 = 1.34 C44 = 1.16 [48]

Anomalous absorption coefficient : ANO = 0.07

[0 0 1] is not in agreement with the experimental image (d). On these ground, the Burgers vector of dislocation 'A' is unlikely to be either of these possibilities and a further comparison of the remaining computed and experimental images confirms this conclusion. However, it can be seen that visual agreement is sufficient to conclude that the most likely Burgers vector for dislocation 'A' is ½ [101].

2.6 Summary

Mechanical testing (compression) of heat treated single crystal NiAl alloys shows that the yield stress increases as the cooling rate through the critical temperature region decreases.

The slip trace analysis shows (001) to be the glide plane for all the specimens.

TEM examination of both deformed as well as undeformed specimens show the following observations and analysis;

- Both < 0 0 1 > and < 0 1 1 > types of dislocations were observed although dominantly <0 0 1> type.
- 2. Irrespective of heat treatment histories and yield strengths, dislocations were observed to move under the influence of the electron beam suggesting that the dislocations in the structure are mobile.
- 3. Undeformed specimens, irrespective of heat treatment histories, display similar dislocation densities. Single dislocations were observed to be widely spaced with few dislocation tangles.
- 4. Deformed specimens having higher yield stress (and hence lower fracture toughness) display extensive dislocation tangles whereas those with lower

yield stress (and hence higher fracture toughness) show fairly straight dislocations. These dislocation tangles are a result of deformation during compression test.

- 5. In the deformed specimens, dislocations were observed to be restrained when they moved into dislocations that were tangled. These dislocation tangles act as an obstacle to dislocation motion and are a hindrance to the movement of the mobile dislocations in the structure.
- 6. Deformed specimens displaying heavily tangled dislocations had undergone furnace cooling whereas deformed specimens which do not show much dislocation tangles had been rapidly cooled. This leads to the possibility that with slow cooling, there is sufficient time for interstitial atoms to diffuse to positions at or near the cores of dislocations and results in strain aging embrittlement. As a result, the pre-existing dislocations are immobilized. This influenced the mobile dislocation density.

CHAPTER 3

SEM EXAMINATION

3.1 Introduction to electron channeling contrast imaging (ECCI)

This section deals with examining the brittleness problem in NiAl. This problem may be associated with difficulty in the generation of fresh dislocations and the ability to move these dislocations, particularly at the highly stressed regions of crack tips. To understand this dislocation generation and mobility, the present study examined the dislocation behavior near crack tips using electron channeling contrast imaging (ECCI), a scanning electron microscope (SEM) technique. This technique has gained attention as a potential method for imaging near surface crystal defects (for reviews, see ref. 40-44). Although in-situ straining transmission electron microscopy (TEM) [45-47] and atomic force microscopy (AFM) [48] have in the past been used to study the dislocation behavior near crack tips, the ECCI technique provides certain characteristic features that are unmatched by both TEM and AFM. ECCI allows experiments to be performed on bulk specimens as opposed to TEM. Thus ECCI has the potential to overcome the difficulties associated with the thin foils used in TEM, including the complications of specimen preparation, surface effects coupled with the strong interaction between the crack tips and dislocations, and the unknown stress state at the crack tip. The limitation of the AFM approach to assessing dislocations near crack tip is that it estimates the number of dislocations within a slip plane by measuring the slip step height as a function of distance from the crack tip [48] and is thus an indirect approach to studying dislocations. It does not provide the kind of visual information about the dislocations near the crack tips that is revealed by the ECCI technique.

The ECCI technique may be best understood by examining the source of the contrast, namely electron channeling. The basis behind electron channeling is that the backscattered electron (BSE) yield from a perfect crystal is dependent on the angle of incidence of the electron beam relative to the numerous Bragg conditions within the crystal. The BSE yield undergoes a significant change upon crossing the Bragg condition [49-51]. When the general bulk specimen is tilted such that it is at one of the Bragg conditions, then any near surface defects will cause a change in the BSE yield, due to variations from the Bragg conditions (Figure 27). The BSE yield from the tilted volume will be different from the rest of the crystal, thus highlighting the local strain field (for instance) of a defect. The reason for the near surface sensitivity is that the electrons from the incident beam loose coherency in penetrating the crystal, and provide less contrast the farther in they travel, limiting the depth of detection [52,53]. The basis for ECCI is thus somewhat analogous to the imaging of dislocations in scanning transmission electron microscopy (STEM), or the diffracting plane tilt model of dislocation contrast for the TEM, in that the contrast from defects will give rise to changes in the local diffracting conditions.

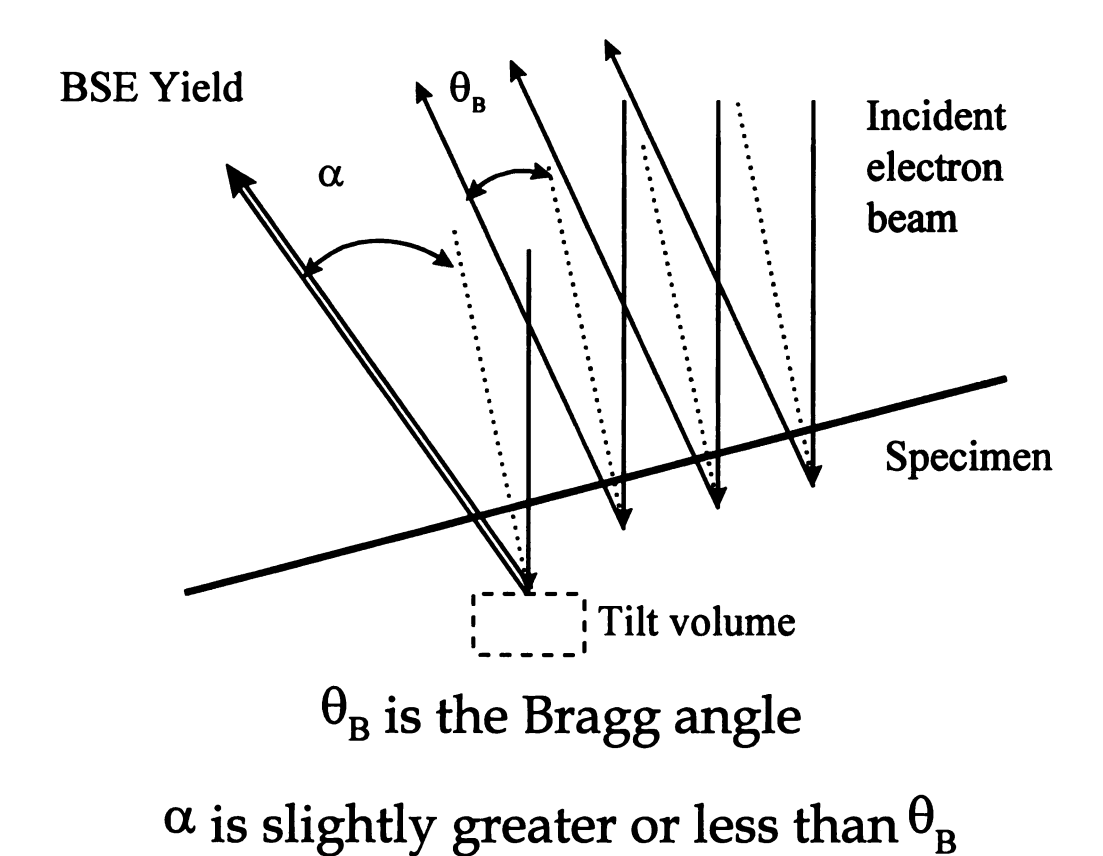


Figure 27. Near surface defects will cause a change in the BSE yield due to variations from the Bragg condition.

Electron channeling patterns (ECPs) are formed by rocking the electron beam about two perpendicular axes on the sample and displaying the resultant BSE signal as a function of tilt angle (Figure 28). This can be accomplished by using a dedicated set of scan coils to rock the beam through the desired range of angles while it is confined to a very small area on the specimen (Figure 29). A pattern captured in this way is referred to as a Selected Area Channeling Pattern (SACP). Actual ECCI imaging is performed using a rastering beam but SACPs are necessary to set up the channeling conditions for ECCI, much like a selected area diffraction pattern is used to set up a two beam diffracting condition for TEM imaging.

3.2 Experimental Procedure

Commercial purity single crystals of NiAl were oriented to $\{0\ 1\ 0\}$ using both Laue back-reflection x-ray and SACP, and then cut to nominal dimensions of 4 x 4 x 20 mm using electro-discharge machining, EDM. The specimens were then subjected to a homogenization heat treatment at 1590 K for 48 hours followed by a slow furnace cool (specimens denoted as 1590FC). Some of these specimens were then retreated at 673 K for 12 hours and either furnace cooled (673FC) or air cooled (673AC). The specimens were mechanically ground and polished to 0.3 μ m using SiC and Al₂O₃ polishing media. The samples were then notched in a $\{0\ 1\ 0\} < 1\ 0\ 0 >$ fashion using EDM, where the given plane represents the plane of the notch and the given direction denotes the direction of the notch (Figure 30).

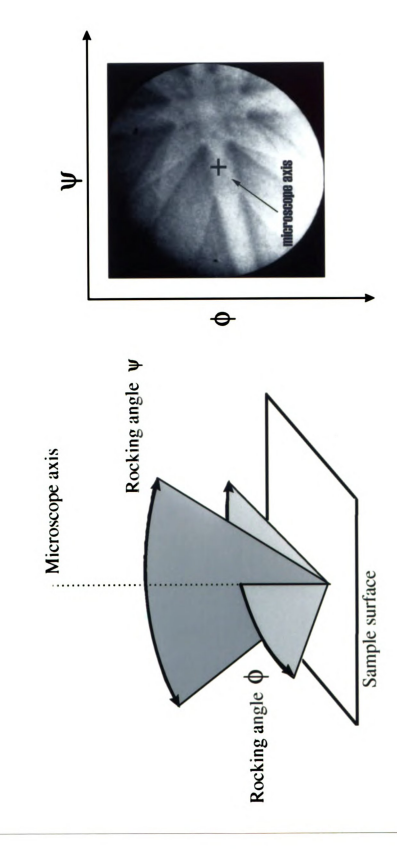


Figure 28. Selected area channeling pattern (SACP)

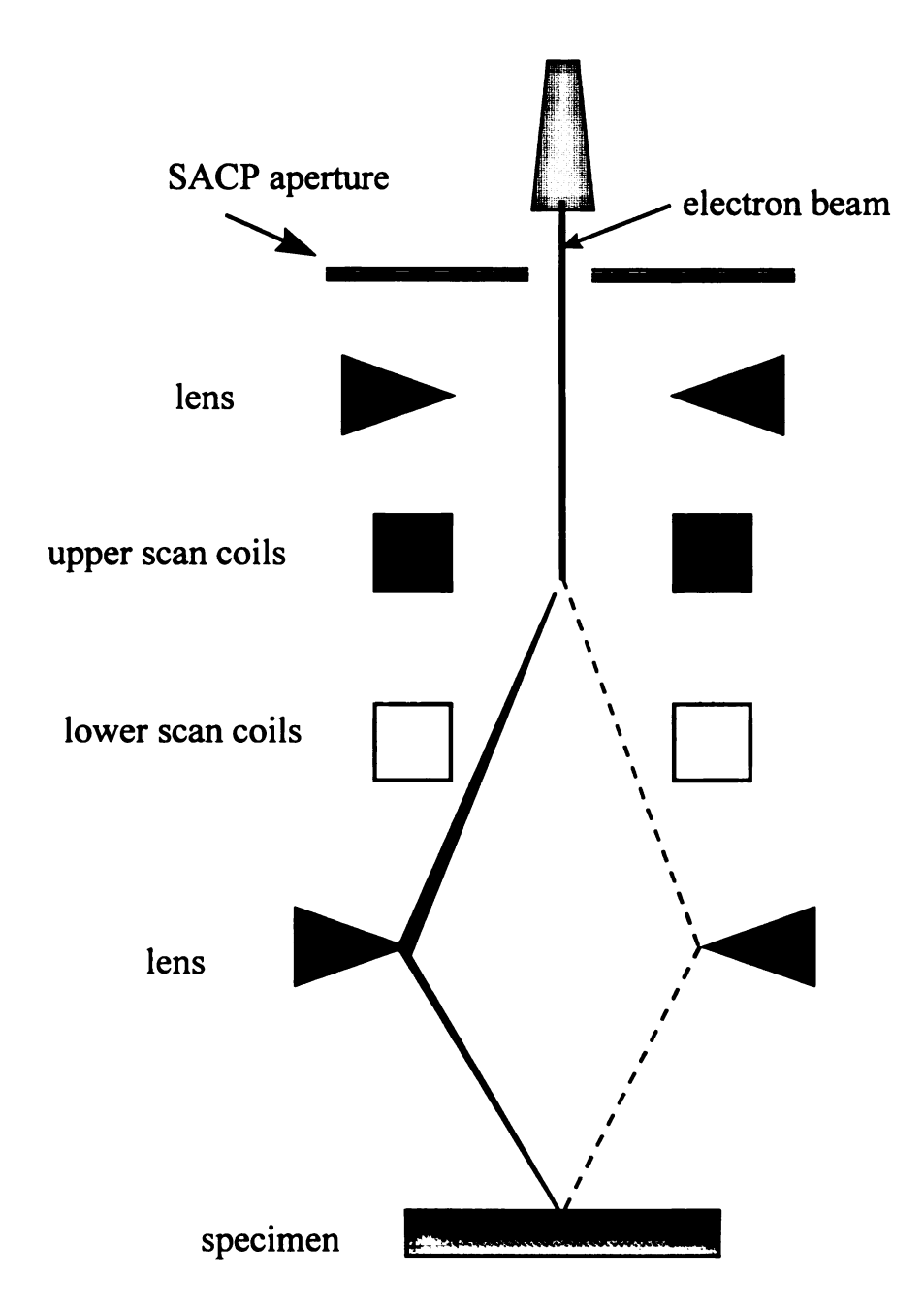


Figure 29. Ray diagrams illustrating schematically the scanning action in the selected area channeling pattern (SACP).

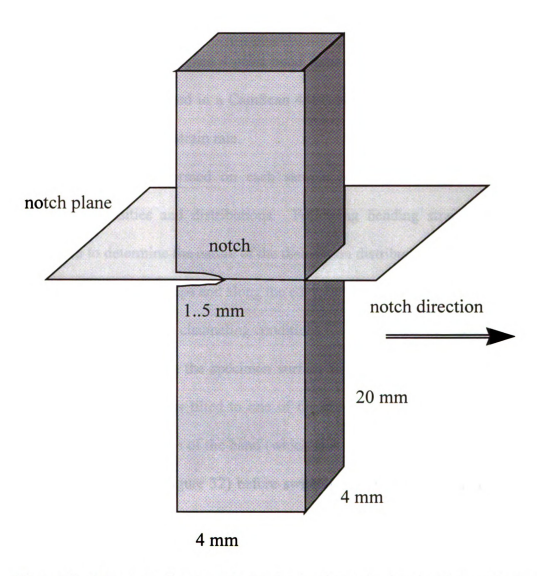


Figure 30. Schematic diagram of a 4 point bend sample showing the notch plane and the notch direction.

The notched specimens were electropolished at 195 K in a solution of 90v.% methanol and 10v.% nitric acid for approximately 60 minutes. Each specimen was then placed in a specially designed 4 point bend fixture attached to a E. Fullam deformation stage (Figure 31) mounted in a CamScan 44FE FEG-SEM. Bending was performed at the minimum attainable strain rate.

ECCI was performed on each sample prior to loading to assess the initial dislocation densities and distributions. Following bending strain, the samples were reassessed to determine the nature of the dislocation distribution. Particular attention was paid to areas near crack tips and along the edges of cracks.

In order to set up channeling conditions for ECCI imaging, the electron beam was rocked about a point on the specimen surface to obtain a SACP. Using the obtained SACP, the specimen was tilted to one of the channeling bands. Final adjustment was made by placing the edge of the band (which is at the Bragg condition [43,54]) onto the microscopic axis (see Figure 32) before switching to the imaging mode. In the present study, ECCI was conducted employing { 1 1 0 } and { 2 0 0 } channeling bands for contrast.

3.3 Results

Specimens deformed using in-situ 4 point bend testing did not exhibit any visible crack extension prior to fracture. In all cases, no crack initiation or propagation was observed prior to catastrophic failure, which occurred via rapid crack motion. As such,

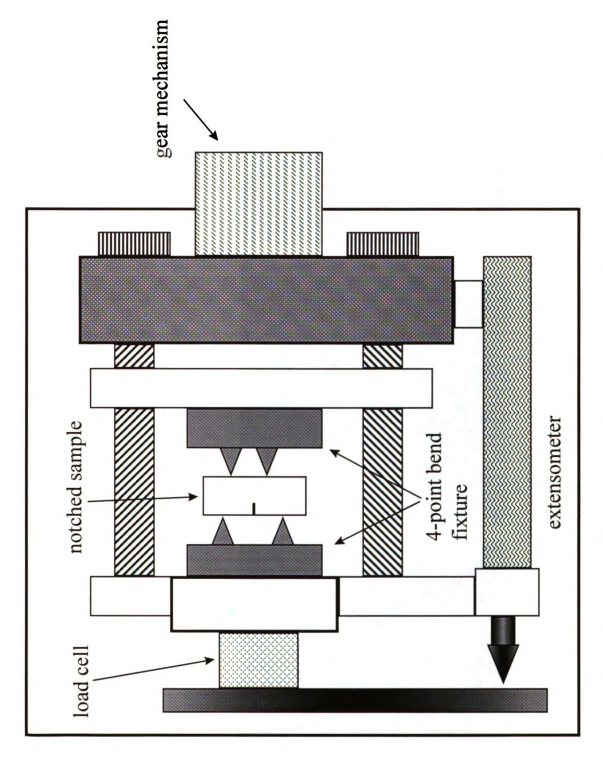


Figure 31. Schematic diagram showing the sample loaded onto the 4-point bend fixture attached to a E. Fullam deformation stage.

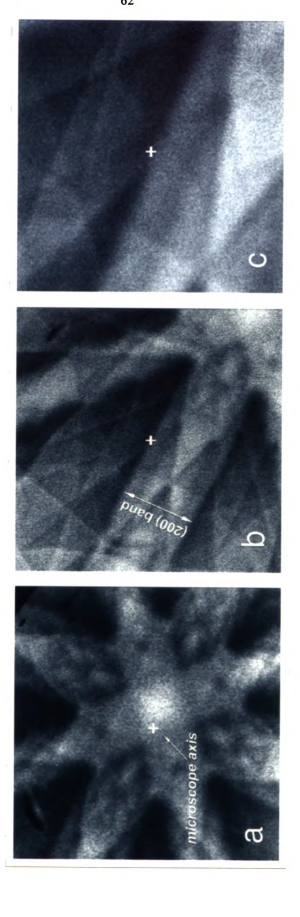


Figure 32. SACP showing a) zone axis, b) tilting to one of the channeling bands, c) final adjustment of aligning the edge of the band (Bragg condition) to the microscope axis.

observations of crack tip regions were made on secondary cracks protruding out from the main fracture crack.

A crack tip in a deformed 673AC specimen is shown in Figure 33 under different imaging conditions. The inserted image shown in Figure 33a is a low magnification secondary electron image (SEI) showing the secondary crack and highlighting the region to be analyzed. Due to the lack of topographic features, the SE image of the crack tip in Figure 33a shows low contrast, whereas the ECCI image of the same crack region in Figure 33b shows dislocations lying roughly end-on with one end of each dislocation exiting the crystal. These dislocations appear somewhat similar to the contrast displayed by end-on dislocations in thin TEM foils [55]. The dislocations decrease in contrast as they penetrate deeper into the sample. This is because the electrons from the incident beam loose coherency in penetrating the crystal and hence provide less contrast the farther in they travel. In this sample, dislocations are observed only within a few microns of the crack tip and edges. These dislocations serve to shield the crack tip and hence increase the macroscopic fracture toughness of the material. The crack in the ECCI image appears different from the SE image because electrons will continue to penetrate deeper into the crack with little or no backscattered electrons escaping the crystal leading to a low BSE signal.

Figure 34 shows SE and ECCI images of a crack edge in a 1590FC specimen. The ECCI image reveals dislocations and cracks that are not visible in the SE image. It is apparent that dislocation generation has occurred along the crack path. The ECCI image reveals that dislocations lie end-on as well as parallel to the surface, and are limited to a

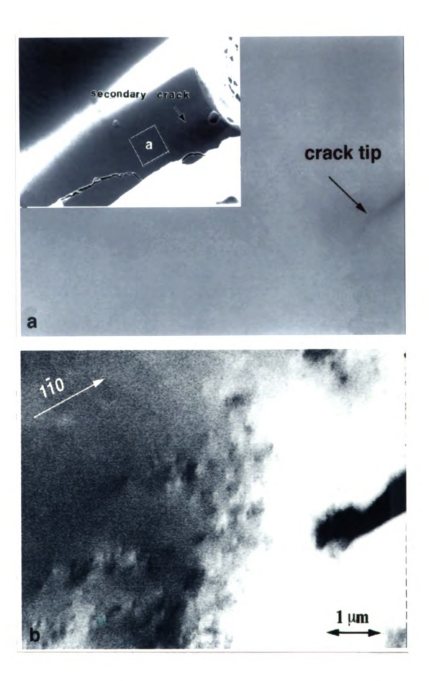


Figure 33. Crack tip in deformed specimen 673AC under different imaging conditions.

a) High magnification SE image of the crack tip region. Inserted image shows a low magnification SE image of the secondary crack and highlighting the area analyzed.

b) ECCI image of the crack tip region showing dislocations lying end-on.

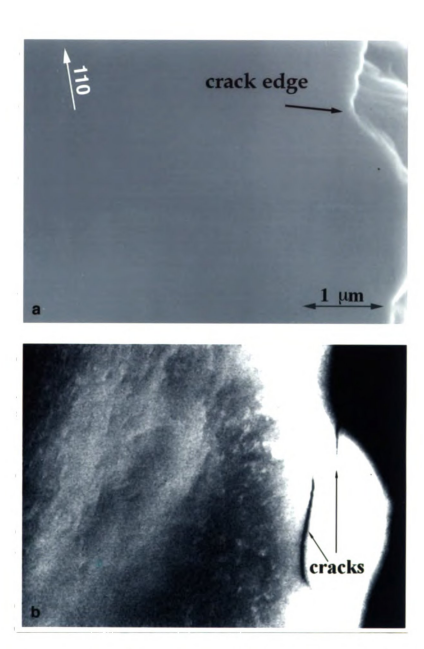


Figure 34. Examples of dislocation distribution left in the wake of the cracks for 1590FC specimen. a) SE image of the crack edge. b) ECCI image of the same crack edge region.

region within ~ 4-μm of the crack. A thin bright band is observed near the edge of the crack. One possible reason for this bright band is the result of the edge effect. Figure 35 shows a schematic representation of the interaction volume within the specimen and near the edge of the specimen. As shown, backscattered electrons can escape easily through the edge and hence result in a higher BSE. In contrast, backscattered electrons generated away from a edge must escape through the surface, consequently there will be a lower BSE yield. However, dark bands at crack edges have also been observed. This may be rationalized by considering the possible effects of mode I and II failure, where the surface may be tilted (Figure 36) leading to a local change in channeling conditions (this could result in either a higher or lower BSE yield).

Figure 37 shows SE and ECCI images of an edge of the crack of 673AC specimen, in this case, with a dark band near the crack edge. Most of the dislocations are seen to be lying end-on. The bright region with some dark patches is indicative of the cumulative strain field of the clusters of dislocations in the region. This suggests a third possibility that the bright band could also be a result of numerous dislocations at the edge, resulting in a cumulative ECCI effect [43]. A noticeable feature of the ECCI micrograph is that more than a few microns from the crack, there are hardly any dislocations. While propagation of a crack clearly leads to an increased dislocation density in the local crack region, the four-point bending does not generally lead to dislocation generation away from the crack regions.

- electron beam-BSE yield stronger BSE yield BSE yield edge of specimen

specimen

Backscattered detector

Figure 35. A higher BSE yield resulted when the rastering beam is near to a edge of a specimen.

interaction

volume

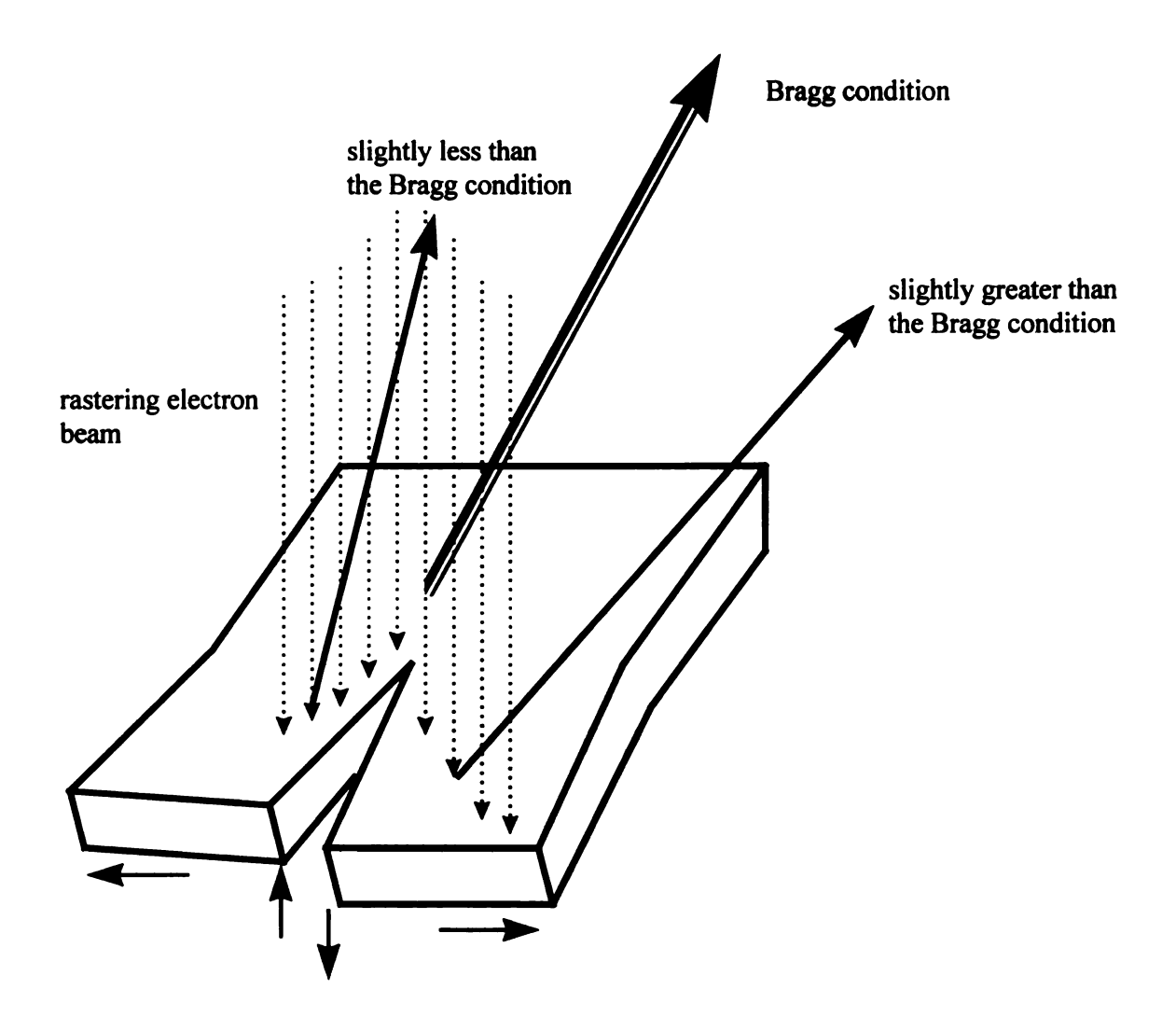


Figure 36. Schematic diagram showing how the combination of mode I and II tear results in a change in the BSE yield for both sides of the crack edge.

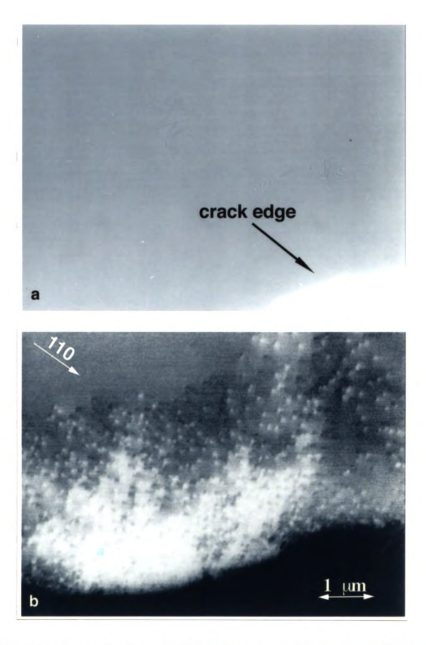


Figure 37. Images of a crack edge of a 673AC specimen illustrating a) SE image and b) ECCI image with dislocations in dark/bright contrast lying end-on.

A comparison of dislocation densities a few tens of microns away from the crack before and after the deformation showed no significant change in the dislocation density. As shown in Figure 38, both micrographs show the same dislocations (arrowed). As expected, it appears that the dislocations generated in 4-point bend testing are limited to regions very close to the cracks. The difference in the contrast of the two images is due to differences in channeling conditions used to form the images. General observation of the specimens shows that the toughened materials (673AC) displayed a significantly higher dislocation density over a larger region in front of the crack tip than the brittle materials (1590FC). This can be seen in Figure 39 where the dislocation density and distribution in front of the crack tips of the brittle materials, 1590FC, are less than that of the toughened material, specimen 673AC.An interesting observation using the ECCI technique is that by changing the channeling conditions between positive (+) g and negative (-) g subsurface defects can be distinguished as to a dislocation or microcrack. Dislocation images will display a dark/bright contrast or a bright/dark contrast image pairs (Figure 40) as a result of the change in the (+) or (-) channeling condition. This change in appearance is somewhat similar to that observed between darkfield and brightfield images commonly used in TEM. However, the actual contrast mechanisms are quite different. Cracks on the other hand do not show changes in contrast with changes in channeling conditions as the electron beam will penetrate deeper into the surface and hence cracks will continue to appear dark (as in Figure 41) in all channeling conditions.

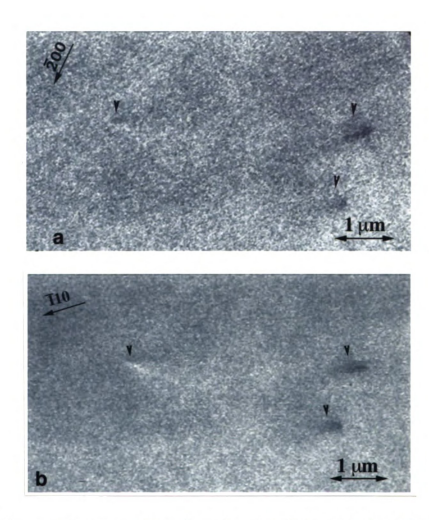


Figure 38. Images of an area $80~\mu m$ from the edge of the crack for 673AC specimen before (a) and after (b) 4-point bend test. No significant change in the dislocation density was observed.

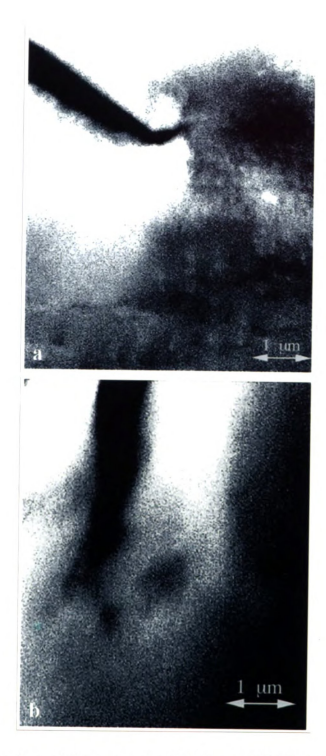


Figure 39. Comparison of dislocation densities for a) 673AC specimen, b) 1590FC specimen.

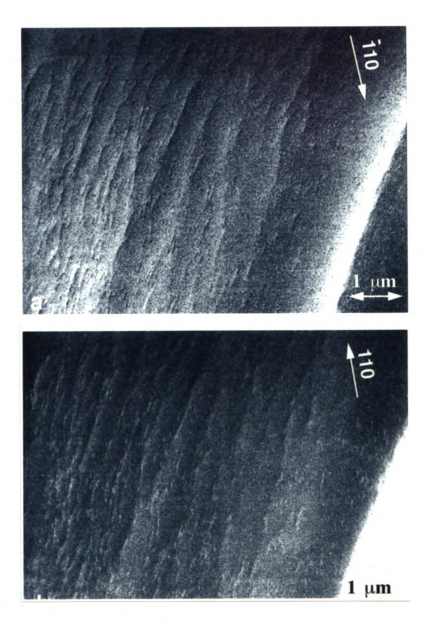


Figure 40. Changes in contrast of dislocation images when the channeling band is changed from a) + g to b) - g.

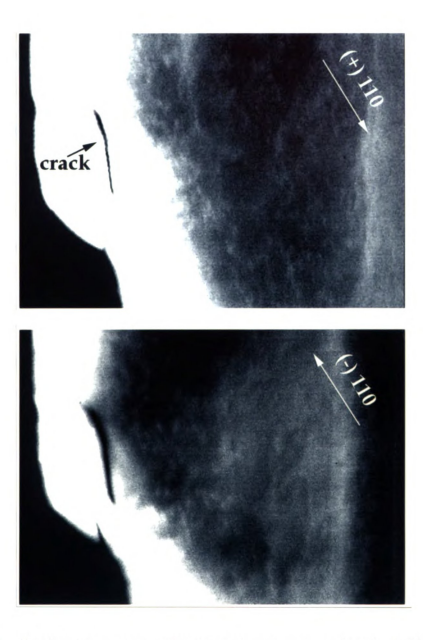


Figure 41. Cracks do not show any change in contrast as the channeling condition changes from +g to -g.

3.4 Summary

The use of the electron channeling contrast imaging (ECCI) technique to image dislocations near crack tips in bulk NiAl single crystal 4-point bend specimens has led to the following observations:

- A higher dislocation density was observed over a larger region in front of the crack tip for the toughened materials as compared to the brittle materials.
- Although a different contrast mechanism is used in ECCI, dislocations observed near
 the crack tips using this technique appear somewhat similar to images of dislocations
 lying normal to TEM thin foils.
- A bright or dark region along crack edges and in front of crack tips is believed to be due to the local tilt of the crystal at the crack edge/tip. This local tilt may be a result from a number of mechanism. Dislocations originating from the crack could change the channeling condition resulting in a higher BSE signal. Backscattered electrons escaped though the crack edges instead escaping through the surface thus resulting in a higher BSE yield. The same band could also be a result of the combination of mode I and II failure causing the crack surface to be tilted such that the resultant BSE yield from the tilted edge will be greater or less than the surrounding area, thus resulting in the change of contrast.
- It was observed that the dislocation density was essentially unchanged in regions more than a few microns from the crack path. Consequently, it appears that the dislocations generated by 4-point bend testing are limited to regions close to the crack, even in toughened materials.

• Changing the channeling conditions from (+) g to (-) g result in dislocation images that are similar to brightfield/darkfield images obtained in TEM.

CHAPTER 4

DISCUSSION

In chapter 2 and 3, TEM and ECCI examinations of dislocation mobility and generation in single crystal NiAl have been presented. In this section, these results will be used to explain the observed mechanical behavior of these NiAl alloys.

Previous studies have clearly shown that the room temperature ductility and toughness of NiAl are strongly influenced by controlled heat treatment, use of superimposed hydrostatic pressure, microalloying with agents, and/or by the presence of interstitial impurities. These studies have lead to the proposition that NiAl and BCC metals having significant levels of interstitial impurities, are subject to a strain aging phenomenon.

It is clear from both the TEM and ECCI results that changes in thermal treatment have an effect on the observed dislocation mobility and distribution in NiAl single crystals. It is of interest to attempt to relate these observations to the general understanding of strain aging in this material.

In the TEM examination, it was observed that air cooled specimens displayed lower yield strengths but correspondingly higher fracture toughnesses in contrast to furnace cooled specimens which tended to display higher yield strengths but were correspondingly very

brittle. Furthermore, the deformed specimens showed vast differences in the gross dislocation morphology and densities depending on whether they had been air cooled or furnace cooled. Furnace cooled specimens displayed dislocations that were heavily tangled, whereas air cooled specimens exhibited fewer dislocation tangles. However, the gross dislocation morphology and densities prior to deformation were the same irrespective of heat treatment histories and cooling rates. Additionally, dislocations in both the deformed and undeformed specimens were observed to move under the influence of the electron beam regardless of pre-deformation cooling rate. This suggests that dislocations are mobile in NiAl regardless of thermal history. However, as the dislocations which glided under the influence of the electron beam moved into dislocation tangles, they were found to be restrained from moving further and piled-up with the rest of the dislocations in the tangles.

A possible explanation for the vast differences in the gross dislocation morphology of the deformed specimens is the cooling rate used. It should be recalled that commercially pure single crystal NiAl alloy, which has significant levels of interstitial elements, was used in this study. It is likely that in specimens that have been slow cooled, interstitial atoms have sufficient time gettering to diffuse into the cores of dislocations, resulting in pinning of the existing dislocations and leading to restricted mobility. When such a specimen is then deformed, newly generated dislocations, which themselves may not be pinned, will however be restrained by the rest of the pinned pre-existing forest of dislocations. This leads to increases in dislocation pile-ups, dislocation tangles and the accumulation of more forest dislocations, resulting in increases in yield stress and consequently, a lower ductility. This is essentially a static strain aging phenomenon as it is the dislocations which are pinned prior to deformation which are responsible for the yield strength increase. In contrast, fast cooling

'traps' the interstitials in solution and as such pre-existing dislocations are not subject to the static strain aging and are free to move. When these fast cooled specimens are deformed, newly generated dislocations and pre-existing dislocations will encounter fewer obstacles, thus resulting in a lower yield stress and higher ductility for the material.

The actual interstitial agents responsible for the strain aging phenomenon have not been determined in the present study. However, Weaver [21] has extensively investigated the strain aging phenomenon in NiAl. Through a systematic study using several nominally stoichiometric polycrystalline and single crystal alloys containing varying interstitial contents, it was concluded that the major solute responsible for pinning the dislocations in NiAl is carbon.

In this present study, commercial purity single crystal with an average of 100 wppm of carbon and 50 wppm of oxygen were examined [8,9,13]. The large amount of impurities/interstitial atoms present provide a good opportunity for static strain aging to occur. However, with a significant reduction in the concentrations of interstitial agents, as in high purity materials, it is believed there will be less pinning of the pre-existing dislocations. This will decrease the susceptibility of NiAl to the static strain aging phenomena as pre-existing dislocations will remain mobile despite slow cooling. Consequently, high purity materials should have higher ductilities and fracture toughnesses. This has been demonstrated by Levit et al. [19] who have achieved elongations of ~25% in high purity materials. In a separate study employing in-situ straining TEM, Ghosh and Crimp [57] further reinforced the concept of strain aging in commercial purity NiAl when they observed the motion of dislocations in commercial purity single crystals NiAl to be 'slow and progressive' versus very rapid in high purity materials. This slow and progressive motion of

purity single crystals NiAl to be 'slow and progressive' versus very rapid in high purity materials. This slow and progressive motion of the dislocations in commercial purity alloys is believed to be a consequence of solute drag (dynamic strain aging). In the high purity single crystal NiAl, the lower interstitial contents lead to a much lower degree of dynamic strain aging.

While TEM examinations indicate that static strain aging plays a role in the effect of thermal treatments, ECCI images, showing decreased crack tip plasticity in brittle materials, have not been able to specifically determine if a static strain aging phenomena is involved, or if some other effect, such as interstitial embrittlement, is responsible for decreased dislocation generation. Nevertheless, ECCI images provide important information on how the effect of thermal treatment affects the crack tip plasticity.

The ECCI observations show that in the air cooled specimens (toughened) the dislocations ahead of the crack tips were more widely distributed (~4 µm ahead of the crack tip) than furnace cooled specimens (~2 µm ahead of the crack tip) (refer to Figure 39). This suggests that it is more difficult to generate fresh dislocations at the highly stressed region of the crack tip in furnace cooled specimens. When dislocation generation is difficult, ductility can suffer if pre-existing dislocations cannot provide sufficient plastic deformation to relax the crack tip.

The sparse distribution of dislocations observed in front of crack tips in the furnace cooled specimens might also another possibility. Assuming that new dislocations can be generated at crack tips in both the air cooled and furnace cooled materials, then differences in the pre-existing dislocations described above may result in differences in the observed dislocation behavior at crack tips. The large number of dislocations

observed in front of crack tips of air cooled specimens would then suggest that newly generated dislocations, with fewer pinned dislocations or dislocation tangles ahead of them, are able to move further away from the crack tips and are more readily observed by ECCI. In contrast, if dislocations are pinned very close to the crack tips, as in the furnace cooled materials, these dislocations might fall within the bright or dark bands near the crack tip, making the dislocations difficult to observe.

When a crack tip emits dislocations, these newly generated dislocations must move out of the crack tip region. But with dislocation tangles resulting from solute pinning the dislocations in furnace cooled materials, these dislocation tangles may hinder the emission of dislocations from the crack tips as the dislocations will be block by the dislocation tangles. As a result, fewer dislocations move out of the crack tips. This may be what was observed in the ECCI images for furnace cooled materials. With fewer dislocations emitting out of the crack tip, there will be less plastic deformation and crack blunting and hence cracks continue to propagate and this results in brittle fracture.

In general, this study demonstrates that TEM and ECCI can play complementary roles in assessing the role of dislocations in controlling the mechanical response of the material. TEM provides the microstructural information on how the dislocation mobility is hindered by forest of dislocations as a result of static strain aging. ECCI, on the other hand, shows dislocation distributions ahead of the crack tip region. These dislocation distributions are indicative of the crack tip plasticity. Relative toughness or brittleness of a material may be estimated by noting the extent of plasticity surrounding the crack tip. [58].

CHAPTER 5

GENERAL CONCLUSION

This study examines the types of dislocations, their behavior, as well as the dislocation distribution in the region of the crack tips and crack edge, of single crystal stoichiometric NiAl.

- Slip trace analysis revealed (001) to be the glide plane for all the specimens.
- TEM examination of both deformed as well as undeformed specimens showed that both < 0 0 1 > (dominant) and < 0 1 1 > dislocations were present in toughened as well as the embrittled specimens. This suggest that it is not the type of dislocation present that result in the change in the properties of toughness or brittleness of the material.
- Irrespective of heat treatment histories and yield strengths, dislocations were observed to move under the influence of the electron beam suggesting that the dislocations in the structure are mobile.
- TEM observations of deformed slow cooled specimens showed dislocation tangles or forest of dislocations, while fast cooled specimens exhibited very few dislocation tangles. Dislocations were observed to be restrained when they move into these tangles. This suggests that the dislocation tangles are obstacles to

dislocation motion. These dislocation tangles are a result of static strain aging where the interstitial atoms diffuse into the cores of the dislocations and pin them.

As a result, the pre-existing dislocations are immobile.

- be imaged. Examinations of crack tips and crack edges showed that fast cooled specimens displayed a higher dislocation density over a larger region in front of the crack tips than the slow cooled specimens. This dislocation distribution ahead of the crack tip is indicative of the crack tip plasticity. Furnace cooled specimens have higher crack tip plasticity.
- Lastly, TEM and ECCI play complementary roles in assessing the role of dislocations in controlling mechanical response of material.

REFERENCE

- 1. D.P. Pope and R. Darolia, MRS Bulletin/May 1996, Vol. 21, No. 5, pp. 30-36.
- 2. R. Darolia, JOM 43 (1991) pp. 44-49.
- 3. J.H. Westbrook, MRS Bulletin/May 1996, Vol. 21, No. 5, pp. 26-28.
- 4. P. Nash, M.F. Singleton and J.L. Murray, Phase Diagrams of Binary Nickel Alloys, Vol. 1, ASM International, Metals Park, Ohio (1991).
- 5. D.R. Miracle, Acta metall. mater., 41, No.3 (1993), pp. 649-684.
- 6. C.T. Liu, and J. A. Horton Jr., Materials Science and Engineering A, 192/193 (1995) pp. 170-178.
- 7. B. Zeumer, W. Wunnike-Sanders, G. Sauthoff, Materials Science and Engineering A, 192/193 (1995) pp. 817-823.
- 8. J.E. Hack, J.M. Brzeski and RD. Field, Scripta Met. et Mat., 27, (1992) pp. 1259-1263.
- 9. J.E. Hack, J.M. Brzeski, R. Darolia and R.D. Field, High Temperature Ordered Intermetallic Alloys V, MRS Proceedings, Vol. 288, 1993 MRS, pp. 1197-1203.
- 10. American Society for Metals, Metals Handbook, 9th Ed. Vol. 11, ASM, Metals park, OH (1986).
- 11. D. Hull and D.J. Bacon, "Introduction to Dislocations", 3rd Edition, International series on Materials Science and Technology, Vol. 37, Pergamon Press, (1984), pp. 225.
- 12. A.H. Cottrell, "<u>Dislocations and Plastic Flow in Crystals</u>", Oxford University Press, Amen House, London, 1965.

- 13. J.M. Brezeski, J.E. Hack, R. Darolia and R.D. Field, Materials Science and Engineering, A170 (1993) pp. 11-18.
- 14. R.W. Margevicius and J.J. Lewandowski, Acta metall. mater., Vol. 41, No. 2, (1993) pp. 485-496.
- 15. R.W. Margevicius and J.J. Lewandowski, Scripta Met. et Mat., Vol. 25, (1991) pp. 2017-2022.
- 16. D.S. Liu, M. Manoharan, and J.J. Lewandowski, Scripta mater., 23, (1989) pp. 253-256.
- 17. C.T. Liu, High Temperature Ordered Intermetallic Alloys V, MRS Proceedings. Vol 288, 1993 MRS, pp. 3-19.
- 18. R. Darolia, D.F. Lahrman and R.F. Field, Scripta Met. et Mat., Vol. 26, (1992) pp1007-1012.
- 19. V.I. Levit, I.A. Bul, J. Hu and M.J. Kaufman, Scritpa Met., Vol. 34, No. 12 (1996) pp. 1925-30.
- 20. W.C. Leslie, Eds., Quench and Strain Aging, Vol. 5, MIT Press, Cambridge, MA., 1986.
- 21. M.L. Weaver, "<u>Investigation of Strain Aging in the Ordered Intermetallic Compound β-Nial</u>", A Dissertation, University of Florida, 1995
- 22. S.J. Chang and S.M. Ohr, Journal of Applied Physics, 52, (1981), pp. 7174-7181.
- 23. S.M. Ohr and S.J. Chang, Journal of Applied Physics, 53, (1982), pp. 5645-5651
- 24. S.M. Ohr, Scripta Metall., Vol. 20, (1986), pp. 1501 -1505.
- 25. I.H. Lin and R. Thomson, Acta Metall., 34, (1986), pp. 187-206.
- 26. B.S. Majumdar and S.J. Burns, Acta Metall., 29, (1981) pp. 579-588.
- 27. H.L. Fraser, R.E. Smallman, and M.H.Loretto, Phil. Mag., Vol. 28, (1973), p. 651-665.
- 28. Maria A. Morris, Jean-Francois Perez, and R. Darolia, Phil. Mag., Vol. 69, (1994), pp. 485-506.
- 29. R.D. Field, D. F. Lahrman and R. Darolia, Acta metall. mater., Vol. 39, No. 12, (1991), pp. 2951-2959.
- 30. M.A. Morris, J.F. Perez and R. Darolia, High Temperature Ordered Intermetallic Alloys VI, MRS Proceedings Vol. 364, 1995 MRS, pp. 413-418.

- 31. R.D. Field, D.F.Lahrman and R. Darolia, High Temperature Ordered Intermetallic Alloys IV, MRS. Proceedings Vol. 213, 1991 MRS, pp. 255-260.
- 32. R.D. Field, D.F.Lahrman and R. Darolia, Acta metall. mater., Vol. 39, No. 12, (1991) pp. 2951-2959.
- 33. M.H. Loretto and R. J. Wasilewski, Phil. Mag., 23, (1971) pp. 1311-1328.
- 34. R.D. Field, D.F. Lahrman and R.Darolia, Acta. metall. mater., Vol. 39, No.12, (1991) pp. 2961-2969.
- 35. D.B. Miracle, S. Russell and C.C. Law, High Temperature Ordered Intermetallic Alloys III, MRS Proceeding, Vol 133, 1989 MRS, pp. 225-230.
- 36. M.J. Mills and D.B. Miracle, Acta metall. mater., Vol. 41, No. 1 (1993) pp. 85-95.
- 37. H.L.Fraser, M.H. Loretto and R. E. Smallman, Phil. Mag., Vol. 28, (1973) pp. 667-677.
- 38. D. Hull and D.J. Bacon, Introduction to Dislocations, 3rd Edition, International series on Materials Science and Technology, Vol. 37, Pergamon Press, (1984), pp. 35.
- 39. A.K. Head, P. Humble, L.M. Clarebrough, A.J. Morton and C.T. Forwood, <u>Defect in Crystalline Solids</u>, Vol. 7, ed. S. Amelinckx, North-Holland Pub. Co. (1973).
- 40. J.T. Czernuszka, N.J. Long and P.B. Hirsch, Inst. Phys. Conf., Ser. No 117: Section 10 (1991).
- 41. D.C. Joy, MRS Proceeding, Vol 183, Materials Research Society, (1990), pp. 199-209.
- 42. A.J. Wilkinson and P.B. Hirsch, Phil. Mag., A, 72, No. 1 (1995), pp. 81-103.
- 43. A.J. Wilkinson, G.R. Anstis, J.T. Czernuszka, N.J. Long and P.B. Hirsch, Phil. Mag. A, 68 (1993), pp. 59-80.
- 44. B.-C. Ng, B.A. Simkin and M.A. Crimp, Deformation and Fracture of Ordered Intermetallic Materials III, edited by W.O. Soboyejo, T.S. Srivatsan and H.L. Fraser, The Minerals, Metals and Materials Society, (1996), pp. 337-348.
- 45. S.M.Ohr, Materials Science and Engineering, 72 (1985), pp. 1-35.
- 46. I. Baker, and J.A. Horton, Phil. Mag. A, 67, No 2 (1993), pp. 479-489.

- 47. B. Ghosh and M.A. Crimp, Deformation and Fracture of Ordered Intermetallic Materials III, edited by W.O. Soboyejo, T.S. Srivatsan and H.L. Fraser, The Minerals, Metals and Materials Society, (1996), pp. 349-359.
- 48. M. Goken, H. Vehoff, and P. Neumann, Scripta Met. et Mat., 33 (1995), pp. 1187-1192.
- 49. T. Ichinokawa, M. Nishimura, H. Wada, Journal of the Physical Society of Japan, 36 No. 1 (1974), pp. 221-226.
- 50. D.G. Coates, Phil. Mag., 16 (1967), pp. 1179-1184.
- 51. G.R.Booker, A.M.B. Shaw, M.J. Whelan, and P.B. Hirsch, Phil. Mag., 16 (1967), pp. 1185-1191.
- 52. B.A. Simkin, M.A. Crimp, Proceedings, Microscopy and Microanalysis, edited by G.W. Bailey, J.M. Corbett, R.V.W. Dimlich, J.R. Michael and N.J. Zaluzec, 1996, pp. 140-141.
- 53. J.T. Czernuszka, N.J. Long, E.D. Boyes, and P.B. Hirsch, MRS Proceeding, Vol. 209 (1991), pp. 289-292.
- 54. P.B. Hirsch, <u>Electron Microscopy of Thin Crystals</u>, Robert E. Krieger Publishing Co., Inc., Hungtinton, New York, (1977), pp. 274.
- 55. N.Rusovic and E.T. Heuing, Phys. Stat. Sol. A, 57, (1980), pp. 529.
- 56. J. Goldstein, <u>Practical Scanning Electron Microscopy</u>; <u>Electron and Ion Microprobe Analysis</u>, New York, Plenum Press, 1975.
- 57. B. Ghosh and M.A. Crimp, "TEM in-situ straining and study of dislocations in NiAl", to be published.
- 58. R.W. Hertzberg, "<u>Deformation and Fracture Mechanics of Engineering Materials</u>", 3rd Ed, John Wiley and Sons, 1976.

fracture toughness, whereas fast cooling (air cooled) tends to decrease the yield strength but results in a much higher fracture toughness value. The dislocation structures of each specimen were examined and the Burgers vectors **b** were determined using the **g·b=0** invisibility criterion. Generally dislocations will be invisible when their **b** lies in the reflecting plane. Using two-beam conditions for a series of individual reflections, two such conditions of invisibility should be found. As **b** is common to both reflections, **b** must be the zone axis of the two planes.

2.4.1 Undeformed Specimens

Burgers vector characterization of an undeformed 673FC specimen is shown in Figure 12. The "a" dislocations with $\mathbf{b} = [0\ 0\ 1]$ are observed to be in weak contrast for both $[2\ 0\ 0]$ and $[1\ 1\ 0]$ reflections while the "b" dislocations $\mathbf{b} = [0\ \overline{1}\ 1]$ are observed to be in weak contrast in both $[2\ 0\ 0]$ and $[0\ 1\ 1]$ reflections.

Figure 13 shows micrographs of undeformed 473FC and 673AC specimens exhibiting <001> and <011> dislocations. Likewise, undeformed 1590AC and 1590FC specimens show similar types of dislocations. It is noted that majority of the dislocations displayed in all the undeformed specimens are dominantly <001> type with a few scattered <011> dislocations.

The gross morphologies of all the undeformed specimens show similar dislocation densities. Figure 14 shows micrographs of 473FC, 673FC and 673AC specimens showing single dislocations widely spaced with few dislocation loops and tangles.

:			
1			
•			
·)			
1			

